



# AD Leonis: Radial Velocity Signal of Stellar Rotation or Spin–Orbit Resonance?

Mikko Tuomi<sup>1</sup>, Hugh R. A. Jones<sup>1</sup> , John R. Barnes<sup>2</sup>, Guillem Anglada-Escudé<sup>3</sup> , R. Paul Butler<sup>4</sup> , Marcin Kiraga<sup>5</sup>, and Steven S. Vogt<sup>6</sup>

<sup>1</sup> Centre for Astrophysics Research, School of Physics, Astronomy and Mathematics, University of Hertfordshire, College Lane, AL10 9AB, Hatfield, UK

<sup>2</sup> Department of Physical Sciences, The Open University, Walton Hall, Milton Keynes, MK7 6AA, UK

<sup>3</sup> School of Physics and Astronomy, Queen Mary University of London, 327 Mile End Road, E1 4NS, London, UK

<sup>4</sup> Department of Terrestrial Magnetism, Carnegie Institution of Washington, 5241 Broad Branch Road NW, Washington, DC 20015-1305, USA

<sup>5</sup> Warsaw University Observatory, Aleje Ujazdowskie 4, 00-478 Warszawa, Poland

<sup>6</sup> UCO/Lick Observatory, University of California, Santa Cruz, CA 95064, USA

Received 2017 August 7; revised 2018 February 13; accepted 2018 February 16; published 2018 April 16

## Abstract

AD Leonis is a nearby magnetically active M dwarf. We find Doppler variability with a period of 2.23 days, as well as photometric signals: (1) a short-period signal, which is similar to the radial velocity signal, albeit with considerable variability; and (2) a long-term activity cycle of  $4070 \pm 120$  days. We examine the short-term photometric signal in the available All-Sky Automated Survey and *Microvariability and Oscillations of STars (MOST)* photometry and find that the signal is not consistently present and varies considerably as a function of time. This signal undergoes a phase change of roughly 0.8 rad when considering the first and second halves of the *MOST* data set, which are separated in median time by 3.38 days. In contrast, the Doppler signal is stable in the combined High-Accuracy Radial velocity Planet Searcher and High Resolution Echelle Spectrometer radial velocities for over 4700 days and does not appear to vary in time in amplitude, phase, period, or as a function of extracted wavelength. We consider a variety of starspot scenarios and find it challenging to simultaneously explain the rapidly varying photometric signal and the stable radial velocity signal as being caused by starspots corotating on the stellar surface. This suggests that the origin of the Doppler periodicity might be the gravitational tug of a planet orbiting the star in spin–orbit resonance. For such a scenario and no spin–orbit misalignment, the measured  $v \sin i$  indicates an inclination angle of  $15.5 \pm 2.5$  and a planetary companion mass of  $0.237 \pm 0.047 M_{\text{Jup}}$ .

*Key words:* methods: numerical – methods: statistical – techniques: radial velocities

## 1. Introduction

The Doppler spectroscopy technique has been a successful method for the detection of planets orbiting nearby stars by enabling observers to measure the changes in stellar radial velocities caused by planets orbiting them on Keplerian orbits. For such detection of planets, M dwarfs are especially fruitful targets by being hosts to at least 2.5 planets per star (Dressing & Charbonneau 2015; Tuomi et al. 2018); because their star–planet mass ratios are lower than those for F, G, and K dwarfs and therefore better enable detections of planetary signals; and because they are the most frequent stars in the galaxy and the solar neighborhood (Chabrier & Baraffe 2000; Winters et al. 2015).

Some nearby M dwarfs, such as GJ 581 (Vogt et al. 2010, 2012; Tuomi 2011; Baluev 2013; Robertson et al. 2014), GJ 667C (Anglada-Escudé et al. 2012, 2013; Feroz & Hobson 2013), and GJ 191 (Anglada-Escudé et al. 2014, 2016; Robertson et al. 2015) have been sources of controversy in the sense that different authors have interpreted the observed signals differently or even disagreed in how many signals could be detected. However, the controversial signals in the radial velocities of these targets have very low amplitudes, which necessarily makes their detection and interpretation difficult. This is not the case for AD Leonis (AD Leo, GJ 388, BD +20 2465), which has been reported to experience radial velocity

variations with a period of 2.23 days (Bonfils et al. 2013; Reiners et al. 2013). Both Bonfils et al. (2013) and Reiners et al. (2013) interpreted the 2.23 day periodicity as a signal originating from the corotation of starspots on the stellar surface because the spectra showed line asymmetries that were correlated with the velocity variations. This means that the radial velocities of AD Leo might provide a benchmark case for examining the differences between Doppler signals caused by stellar rotation and planets on Keplerian orbits.

Newton et al. (2016) articulated the detectability challenge that is faced for older M dwarfs. Their range of stellar rotation periods coincides with both the periods where many of their planets lie, as well as with their habitable zones. Therefore, a rotational signal might impersonate a radial velocity signal that would be assigned to a candidate planet. A further consideration is that the rotation period of the star might become locked to the orbital period of the planet and eventually spiral in will occur (e.g., Hut 1980; Adams & Bloch 2015). For *Kepler* stars, there does appear to be a dearth of planets at short orbital periods around fast-rotating stars (McQuillan et al. 2013; Teitler & Königl 2014). Only slow stellar rotators, with rotation periods longer than 5–10 days, have planets with periods shorter than 2 or 3 days (see, e.g., Figure 2 of McQuillan et al. 2013). Teitler & Königl (2014) ran numerical simulations to investigate “why there is a dearth of close-orbiting planets around fast-orbiting stars” and found that this can be attributed to tidal ingestion of close-in planets by their host stars. Finding examples of such stars in the solar neighborhood would then enable studying this mechanism in detail.

In the current work, we analyze the available High-Accuracy Radial velocity Planet Searcher (HARPS) and High Resolution



Original content from this work may be used under the terms of the [Creative Commons Attribution 3.0 licence](https://creativecommons.org/licenses/by/3.0/). Any further distribution of this work must maintain attribution to the author(s) and the title of the work, journal citation and DOI.

Echelle Spectrometer (HIRES) data in order to test the validity of the interpretation that the 2.23 day signal in the radial velocities of AD Leo is indeed caused by stellar rotation rather than tidal locking. In particular, we study the properties of the signal given different models accounting for activity-induced radial velocity variations or not and by examining the dependence of the signal on the spectral wavelength range used to derive the differential radial velocities. We also analyze the All-Sky Automated Survey (ASAS; Pojmański 1997, 2002) *V*-band photometry data and *Microvariability and Oscillations of STars (MOST)* photometry (Hunt-Walker et al. 2012) of the target in order to study the signatures of stellar rotation. Moreover, we attempt to explain the photometric and spectroscopic variability by simulating simple starspot scenarios. Finally, we compare the results to other known rapidly rotating nearby M dwarfs in order to see what, if any, connections there are between photometric rotation periods and radial velocity variations.

## 2. AD Leo

AD Leo (GJ 388) is a frequently flaring (Hunt-Walker et al. 2012; Buccino et al. 2014) M4.5V dwarf with a parallax of  $213 \pm 4$  mas implying a distance of only 4.9 pc. Based on Delfosse et al. (2000) and the *V*- and *J*-band magnitudes, Bonfils et al. (2013) estimated a mass of  $0.42 M_{\odot}$  and a luminosity of  $0.023 L_{\odot}$  as the star was included in their HARPS Search for Southern Extra-Solar Planets program. Given *V* and *J* magnitudes of 9.52 (Zacharias et al. 2013) and  $5.449 \pm 0.027$  (Cutri et al. 2013), we obtain a mass of 0.36 by also applying the relation of Delfosse et al. (2000). According to Houdebine et al. (2016), the star has a radius of  $0.436 \pm 0.049 R_{\odot}$  and effective temperature of  $3414 \pm 100$  K. Neves et al. (2012) estimated the metallicity of AD Leo to be  $[\text{Fe}/\text{H}] = 0.07$ , and Rojas-Ayala et al. (2013) gave a value of  $0.28 \pm 0.17$ .

AD Leo has been claimed to be a photometrically variable star with a  $24 \pm 2$  mmag sinusoidal variability<sup>7</sup> and photometric periodicity of  $2.7 \pm 0.05$  days (Spiesman & Hawley 1986). Although the statistical significance of this periodicity was not discussed in Spiesman & Hawley (1986), they interpreted the result as an indication of the corotation of starspots on the stellar surface and thus, effectively, the rotation period of the star. Based on spectropolarimetry, Morin et al. (2008) reported that the star rotates with a period of  $2.2399 \pm 0.0006$  days (they also gave alternative solutions at periods of 2.2264 and 2.2537 days).

However, the strongest evidence in favor of the short rotation period of AD Leo comes from *MOST*'s photometric observations. *MOST* observations were reported to contain strong evidence for a periodicity of  $2.23^{+0.36}_{-0.27}$  days (Hunt-Walker et al. 2012) caused by “spots distributed at different longitudes or, possibly, that the modulation is caused by varying surface coverage of a large polar spot or a spot that is viewed nearly pole-on.” This suggests a young age, and indeed, Shkolnik et al. (2009) estimated an age of 25–300 Myr. Since the results of Hunt-Walker et al. (2012) were based on a *MOST* photometric time series with a baseline of only 8 days and there was evidence for variation of the parameters of the periodic signal caused by stellar rotation, their results suggest the presence of changing spot patterns that would be unlikely to

<sup>7</sup> To remove ambiguity, we define amplitude such that it denotes parameter  $A$  in  $f(x) = A \sin(x)$ , not  $2A$  as in Spiesman & Hawley (1986).

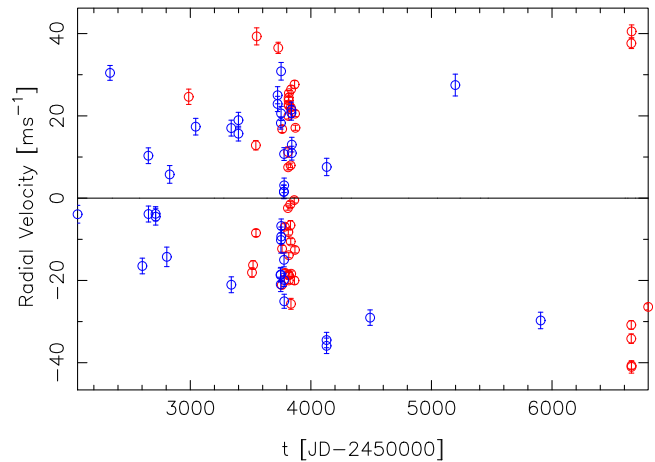


**Figure 1.** HARPS (red) and HIRES (blue) radial velocities of AD Leo with respect to their mean values.

produce stable signals in photometric or spectroscopic data over longer timescales.

AD Leo has been observed to be variable on longer timescales as well. Buccino et al. (2014) reported an approximately 7 yr activity cycle based on ASAS photometry and CASLEO spectroscopy. Although ASAS could not cover a whole period of this cycle and CASLEO detected it only weakly significantly (with a false alarm probability (FAP) of 8%), together they indicate the presence of such a cycle rather convincingly.

It is worth noting that Engle et al. (2009) mentioned a photometric periodicity of 2.23 days (with an amplitude of  $\approx 17$  mmag, judging by their phase-folded plot), but the significance and uniqueness of their solution was not discussed.

The estimated  $v \sin i$  of AD Leo is  $2.63 \text{ km s}^{-1}$  (Houdebine et al. 2016). Together with a radius estimate of  $0.436 \pm 0.049$ , Houdebine et al. (2016) then calculated a projected rotation period of  $8.38^{+1.2}_{-1.1}$  days. Thus, because the rotation period of the star is 2.23 days, this implies inclination of the rotation axis of  $15.5^{+2.5}_{-2.0}$ , which means that the star is oriented nearly pole-on.

## 3. Spectroscopic and Photometric Data

### 3.1. HARPS Radial Velocities

Spectroscopic data of AD Leo were obtained from two sources. We downloaded the publicly available data products of HARPS (Mayor et al. 2003) from the European Southern Observatory archive and processed them with the TERRA algorithms of Anglada-Escudé & Butler (2012). As a result, we obtained a set of 47 radial velocities with a baseline of 3811 days and root-mean-square (rms) estimate of  $22.59 \text{ ms}^{-1}$ . Given a mean instrument uncertainty of  $0.94 \text{ ms}^{-1}$ , there are variations in the data that cannot be explained by instrument noise alone. The majority (28) of these were obtained over a short period of 76 days between JDs 2453809 and 2453871, enabling the detection of the signal at a period of 2.23 days (Bonfils et al. 2013; Reiniers et al. 2013). The HARPS radial velocities of AD Leo are given in Table 1 and plotted in Figure 1.

### 3.2. HIRES Radial Velocities

The second set of spectroscopic data was obtained by the High Resolution Echelle Spectrometer (HIRES; Vogt et al. 1994) of

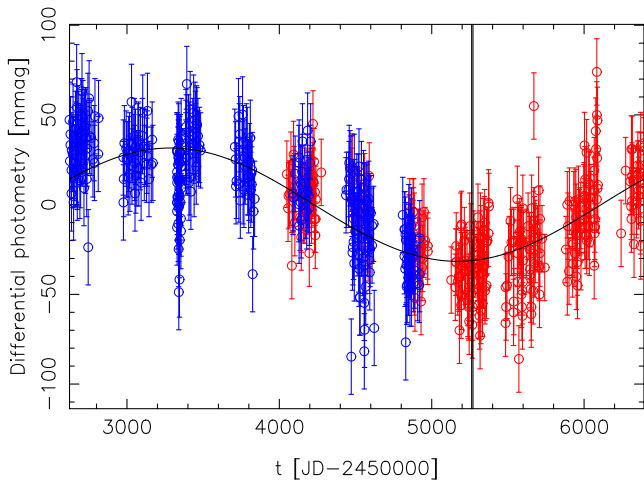


**Figure 2.** ASAS-N (blue) and ASAS-S (red) V-band photometry data of AD Leo with respect to the data mean. Only “Grade A” is shown with all  $5\sigma$  outliers removed. An offset of 25.9 mmag has been accounted for. The uncertainties represent estimated excess variability in the data. The black curve denotes the long-period activity cycle of the star reported by Buccino et al. (2014). The position of the *MOST* observing run is denoted by a vertical line.

the Keck I telescope. This set of 42 radial velocities has a baseline of 3841 days and an rms of  $18.93 \text{ ms}^{-1}$ . With an average instrument uncertainty of  $1.90 \text{ ms}^{-1}$ , this data also indicates excess variability that cannot be explained by pure instrument noise. The HIRES velocities of AD Leo are also shown in Figure 1, as published in Butler et al. (2017).

### 3.3. ASAS Photometry

To study the photometric variability of AD Leo, we obtained ASAS (Pojmański 1997, 2002) V-band photometry data<sup>8</sup> from the ASAS-North (ASAS-N) and ASAS-South (ASAS-S) telescopes. We only selected the “Grade A” data from the set, removed all  $5\sigma$  outliers, and obtained sets of 316 and 319 photometric measurements with baselines of 2344 and 2299 days, respectively. The apertures with the least amount of variability showed brightnesses of  $9263.8 \pm 25.2$  and  $9333.0 \pm 28.3$  mmag. These values are somewhat different, and we thus only compared the two time series by assuming an offset that was a free parameter of the model. The ASAS data are given in Tables 7 and 8 and plotted in Figure 2, together with the estimated long-period cycle that was clearly present in the data as also observed by Buccino et al. (2014). We note that Kiraga & Stepien (2007) did not discuss AD Leo when publishing photometric rotation periods of nearby M dwarfs.

### 3.4. MOST Photometry

We also obtained the raw *MOST* photometry data<sup>9</sup> as discussed in Hunt-Walker et al. (2012). The data are presented in Figure 3 for visual inspection and consist of 8592 individual observations over a baseline of roughly 9 days. The *MOST* observing run is denoted in Figure 2 by a vertical line.

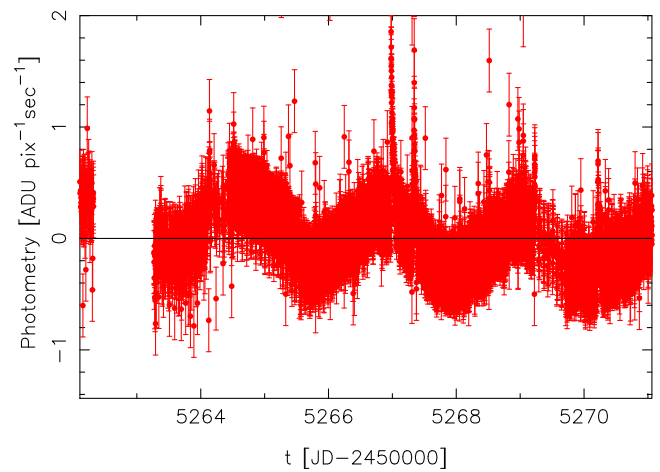


**Figure 3.** Raw *MOST* photometry data of AD Leo with respect to the data mean (see Hunt-Walker et al. 2012, Figure 1). The solid horizontal line represents the data mean.

## 4. Photometric Variability of AD Leo

As observed by Buccino et al. (2014), the dominant feature in the ASAS-S data is a long-period signal caused by the star’s activity cycle. In combination with ASAS-N data, we estimate this cycle to have a period of  $4070 \pm 120$  days when using the standard deviation of the period parameter to describe the uncertainty. The 99% credibility interval of this period is [3730, 4450] days.

Modeling the long-period signal, we analyzed the ASAS photometry of AD Leo by calculating likelihood ratio periodograms of both ASAS-N and ASAS-S data sets. These periodograms were calculated by assuming the measurements were independent and normally distributed. However, instead of the common Lomb–Scargle periodogram (Lomb 1976; Scargle 1982) that is equivalent to the minimization of  $\|C^{1/2}[m - f(\theta)]\|^2$ , where  $m$  is the measurement vector,  $C$  is the covariance matrix, and the model is defined as  $f(\theta) = a_1 \sin \omega t + a_2 \cos \omega t$ , we also included a second-order polynomial such that  $f(\theta) = a_1 \sin \omega t + a_2 \cos \omega t + a_3 + a_4 t + a_5 t^2$  (see also Butler et al. 2017) that thus accounted for the long-period cycle seen as a second-order curvature in the ASAS-N and ASAS-S data sets in Figure 2. In our notation,  $\theta = (a_1, \dots, a_5)$  represents the parameter vector,  $\omega$  is the frequency, and  $t$  is time.

With the model containing a sinusoidal signal and the polynomial terms, we then attempted detecting signals by looking at the likelihood ratios of models with and without the sinusoid (or Keplerian function, when analyzing radial velocities). Our signal detection criteria were such that (i) the signal improved the model significantly, (ii) the signal was unique and well constrained in the period space, and (iii) the amplitude parameter of the signal was well constrained such that it was statistically significantly different from zero (see, e.g., Tuomi 2012). The significance of the signal was determined by calculating the likelihood ratio  $L_r$  of models with and without signals and by seeing if  $\ln L_r > \alpha$ , where threshold  $\alpha$  was set equal to 16.27 for sinusoidal signals (three free parameters) and 20.52 for Keplerian signals (five free parameters), i.e., such that FAP was less than 0.1%. We also calculated whether the signals exceeded detection thresholds such that the model probabilities roughly estimated with the Bayesian information criterion (BIC) increased by a factor of 150 (Kass & Raftery 1995; Feng et al. 2016).

<sup>8</sup> <http://www.astrouw.edu.pl/asas>

<sup>9</sup> *MOST* photometry data were kindly provided by Nicholas M. Hunt-Walker.



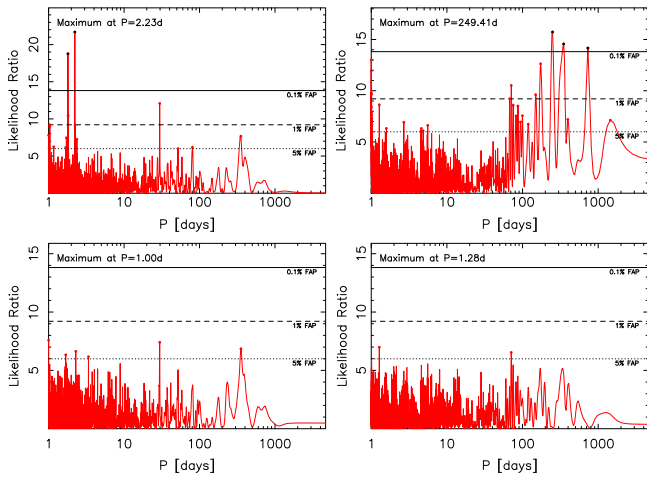


**Figure 4.** Logarithm of the likelihood ratio periodogram of the ASAS-N (left panels) and ASAS-S (right panels) V-band photometry of AD Leo when accounting for the long-period variability seen in Figure 2. The bottom panels show the residual periodogram after subtracting the strongest periodic signal. The red (black) filled circles denote the maxima exceeding the 5% (0.1%) FAP threshold.

The likelihood ratio periodogram<sup>10</sup> of the ASAS-N data shows a maximum in excess of the 0.1% FAP at a period of 2.22791 [2.22736, 2.22857] days with an amplitude of 9.3 [5.2, 13.0], where the uncertainties have been presented as 99% credibility intervals. This periodicity corresponds to the rotation period of AD Leo. No other periodicities could be found in the ASAS-N photometry. Instead, the periodogram of ASAS-S data shows evidence for another period of 257.9 [250.2, 262.5] days with an amplitude of 6.7 [3.0, 11.3] mmag (Figure 4). The secondary periodogram maxima exceeding the 0.1% FAP threshold at periods of 350 and 730 days are likely caused by annual gaps in the data (see Figure 2) and aliasing. After accounting for the long-period cycle, there were no periodicities in the combined ASAS data (allowing an offset between the data sets) exceeding the 0.1% FAP, although four periods—1.81, 2.23, 376.1, and 426.8 days—had likelihood ratios exceeding the 1% FAP threshold.

As can be seen in Figure 4, there is only evidence for the photometric rotation period in the ASAS-N data. This signal is not present in ASAS-S data at all. In particular, the photometric signal at a period of 2.23 days with an amplitude of 9.3 mmag should have been clearly visible in the ASAS-S data, considering that a much longer periodicity of 257.9 days with an amplitude of only 6.7 mmag could be confidently detected. This suggests that when the star reached the brightness maximum corresponding to the long-period activity cycle (Figure 2), the rotation period could not be seen in low-cadence observations such as those obtained by ASAS-S. The *MOST* observations were taken between JDs 2455262.0 and 2455271.0, which corresponds to the brightness minimum as determined by the ASAS data.

We also separately analyzed each of the seven observing seasons (see Figure 2) in order to find periodic signals in them. According to the likelihood ratio periodograms, there was no

evidence for strong periodic signals in excess of 1% FAP in any of the observing seasons. It thus appears evident that although the photometric rotation signal is not strong in the data of any given season, the lack of it in the ASAS-S data suggests it is not very stable, likely due to the fact that spot patterns on the stellar surface differ markedly between different phases of the activity cycle of the star.

#### 4.1. *MOST* High-cadence Photometry

As reported by Hunt-Walker et al. (2012), the *MOST* high-cadence photometry showed clear evidence in favor of a photometric rotation period of 2.23 days, as well as several flare events (Figure 3). In an attempt to obtain constraints for the variability of the photometric signal in the *MOST* data, we split the raw data ( $N = 8592$ ) in half. We then analyzed the two sets to quantify any changes in the phase, period, and amplitude of the photometric signal over the *MOST* baseline of 8.95 days.

According to our results, the phase of a sinusoid changed from  $1.06 \pm 0.08$  to  $1.85 \pm 0.10$  rad (when using standard  $1\sigma$  uncertainty estimates) from the first half of the data to the second. Variability was also detected in the photometric period and amplitude that changed from  $2.289 \pm 0.019$  to  $2.145 \pm 0.011$  days and from  $0.2609 \pm 0.0046$  to  $0.2242 \pm 0.0037$  ADU  $\text{pix}^{-1} \text{s}^{-1}$ , respectively. Given that the median times of the two *MOST* data halves differ by only 3.38 days, this evolution takes place on a timescale comparable to the star’s rotation period. It is thus evident that the spot patterns and active/inactive areas on the star’s surface giving rise to the clear photometric rotation signal experience rapid evolution and change considerably over a period of only a few days.

The variability of the photometric signal on short timescales indicates that the signal detected in ASAS-N data is only an average over a baseline of roughly 3000 days. This implies that the photometric amplitude of the signal detected in ASAS-N appears lower than it actually is because it corresponds to an average over different phases in the star’s activity cycle. This interpretation is supported by Spiesman & Hawley (1986), who estimated the amplitude to be 12 mmag.

## 5. Spectroscopic Variability of AD Leo

The radial velocities of AD Leo were found to vary periodically, as also observed for the HARPS data by Bonfils et al. (2013) and Reiners et al. (2013). We analyzed the data by applying the delayed-rejection adaptive-Metropolis (DRAM) algorithm (Haario et al. 2001, 2006) that is a generalization of the Metropolis–Hastings Markov chain Monte Carlo posterior sampling technique (Metropolis et al. 1953; Hastings 1970). This technique has been used to find periodicities in radial velocity data in, e.g., Jenkins & Tuomi (2014), Tuomi et al. (2014), and Butler et al. (2017).

### 5.1. Activity Indices

We also obtained and analyzed selected HARPS and HIRES activity indicators: the *S*-index measuring the emission of Ca II H & K lines for HARPS and HIRES with respect to the continuum and the line bisector span (BIS) and full width at half maximum (FWHM) for HARPS.

The likelihood ratio periodogram of the HIRES *S*-index showed some evidence (in excess of 5% but not 1% FAP) for a 150 day periodicity (Figure 5, top left panel). This variability could be connected to photometric variability detected in the

<sup>10</sup> We note that the periodograms are calculated for a model with only two additional free parameters because the period parameter is fixed and the 0.1%, 1%, and 5% FAP threshold values are thus at 13.82, 9.21, and 5.99 in the periodograms.

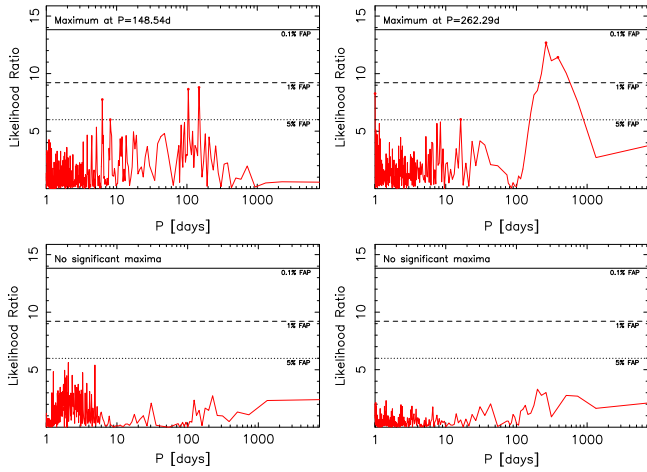


**Figure 5.** Logarithm of the likelihood ratio periodogram of the HIRES  $S$ -index (top left panel), HARPS  $S$ -index (top right panel), BIS (bottom left panel), and FWHM (bottom right panel).

ASAS-S photometry. We also detect a broad maximum in the periodogram of HARPS  $S$ -indices at a period of 300 days (Figure 5, top right panel). However, we could not observe any evidence for periodicities in the HARPS BIS and FWHM values (Figure 5). This result is consistent with that of Reiners et al. (2013), who discussed hints of evidence for periodicities in the HARPS BIS values, but the corresponding periodic signals only barely exceeded 5% FAP in their analyses.

### 5.2. Radial Velocities

We modeled the radial velocities by accounting for a Keplerian signal ( $f_k$ ), reference velocity  $\gamma_l$  of instrument  $l$ , linear trend ( $\dot{\gamma}$ ), linear dependence of the velocities on the activity indices  $\xi_{i,j,l}$  with parameter  $c_{j,l}$ , and moving average component with exponential smoothing accounting for some of the red features (e.g., Baluev 2009; Tuomi et al. 2014) in the radial velocity noise. The statistical model for a measurement  $m_{i,l}$  at epoch  $t_{i,l}$  is thus

$$m_{i,l} = f_k(t_{i,l}) + \gamma_l + \dot{\gamma} + \sum_j c_{j,l} \xi_{i,j,l} + \phi_l \exp\left\{\frac{t_{i-1} - t_i}{\tau}\right\} r_{i-1,l} + \epsilon_{i,l}, \quad (1)$$

where  $\tau$  was set equal to 4 days because we expect to see correlations on that timescale but not on longer timescales (Tuomi et al. 2014) and  $r_{i,l}$  represents the residual after subtracting the deterministic part of the model from the data. The Gaussian random variable  $\epsilon_{i,l}$  represents the white noise in the data: it has a zero mean and a variance of  $\sigma_i^2 + \sigma_l^2$ , where  $\sigma_l$  is a free parameter for all instruments quantifying the excess white noise, or “jitter”, in the data.

The combined HARPS and HIRES radial velocities of AD Leo contained a periodic signal that was clearly identified by our DRAM samplings of the parameter space (Figure 6). We show the HARPS and HIRES radial velocities folded on the phase of the signal in Figure 7 for visual inspection. This signal was supported by both data sets; the maximized log-likelihood (natural logarithm) increased from  $-199.6$  to  $-179.1$  for HIRES and from  $-196.6$  to  $-153.7$  for HARPS, exceeding any

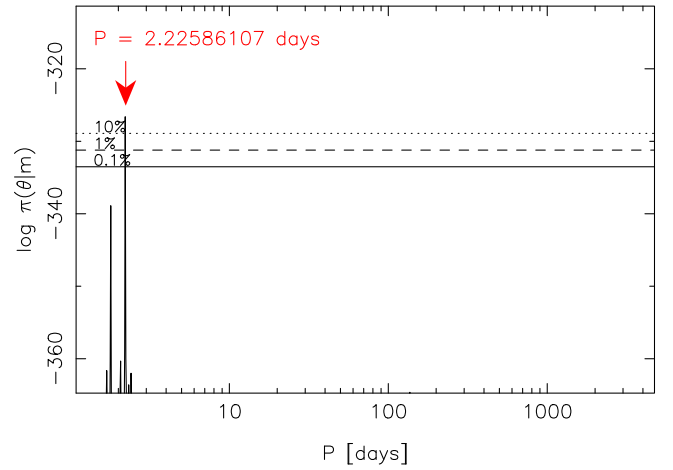


**Figure 6.** Estimated posterior density as a function of the signal period given the HARPS and HIRES radial velocities of AD Leo. The horizontal lines represent the 10% (dotted), 1% (dashed), and 0.1% (solid) equiprobability thresholds with respect to the global maximum denoted by the red arrow.

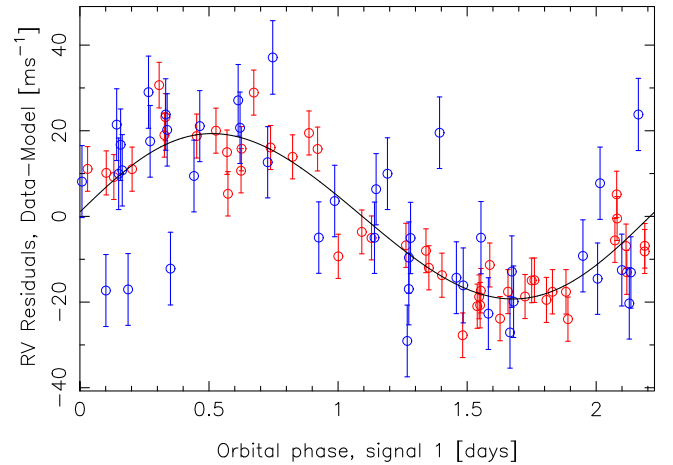


**Figure 7.** HARPS (red) and HIRES (blue) radial velocities of AD Leo folded on the phase of the signal.

reasonable statistical significance thresholds.<sup>11</sup> Using the BIC to determine the significance of the signal (see Schwarz 1978; Feng et al. 2016), we obtain an estimate for the logarithm of the Bayes factor in favor of a model with one signal of 52.25—considerably in excess of the detection threshold of 5.01 corresponding to a situation where the model is 150 times more probable (e.g., Kass & Raftery 1995). This signal satisfied all the signal detection criteria of Tuomi (2012); i.e., in addition to satisfying the significance criterion, it corresponded to a unique posterior probability maximum constrained from above and below in the period and amplitude spaces.

As also reported by Bonfils et al. (2013) and Reiners et al. (2013), we observed a negative correlation between HARPS radial velocities and BIS values. The linear parameter  $c_{j,l}$  (see the model above) that quantifies this dependence of the HARPS velocities on the observed BIS values was found to have a value of  $-2.12$  [ $-2.96, -1.30$ ], which is significantly different from zero at a  $7.7\sigma$  level. Similar strong correlations were not found with HARPS FWHM and  $S$ -index. There was a weaker

<sup>11</sup> For a Keplerian signal with five free parameters, a natural logarithm of a likelihood ratio of 20.52 corresponds to a 0.1% FAP.

**Table 1**

Maximum a Posteriori Estimates and 99% Credibility Intervals of the Parameters of a Model with One Keplerian Signal and with or without Correlations with the Activity Indicators

Parameter	Full Model	No Activity Correlations
$K$ [ $\text{ms}^{-1}$ ]	19.11 [15.69, 22.54]	23.18 [19.68, 26.67]
$P$ [days]	2.22579 [2.22556, 2.22593]	2.22579 [2.22566, 2.22592]
$e$	0.015 [0, 0.147]	0.028 [0, 0.161]
$\omega$ [rad]	4.7 [0, $2\pi$ ]	5.1 [0, $2\pi$ ]
$M_0$ [rad]	6.2 [0, $2\pi$ ]	0.3 [0, $2\pi$ ]
$a$ [au]	0.024 [0.021, 0.026]	0.024 [0.021, 0.027]
$m \sin i$ [ $M_{\oplus}$ ]	19.7 [14.6, 25.3]	23.8 [17.9, 29.8]
$\dot{\gamma}$ [ $\text{ms}^{-1} \text{yr}^{-1}$ ]	-1.50 [-3.00, -0.31]	-1.68 [-2.46, -0.89]
$\sigma_{\text{HARPS}}$ [ $\text{ms}^{-1}$ ]	5.52 [4.27, 6.90]	6.58 [5.36, 8.09]
$\sigma_{\text{HIRES}}$ [ $\text{ms}^{-1}$ ]	8.40 [7.07, 9.88]	8.74 [7.47, 10.31]
$\phi_{\text{HARPS}}$	-0.10 [-0.94, 0.80]	-0.66 [-1, 0.07]
$\phi_{\text{HIRES}}$	0.61 [0.05, 1]	0.27 [-0.39, 0.88]
$c_{\text{BIS,HARPS}}$	-2.12 [-2.96, -1.29]	...
$c_{\text{FWHM,HARPS}}$	0.230 [-0.141, 0.600]	...
$c_{\text{S,HARPS}}$ [ $\text{ms}^{-1}$ ]	-0.14 [-2.82, 2.55]	...
$c_{\text{S, HIRES}}$ [ $\text{ms}^{-1}$ ]	1.62 [0.21, 3.18]	...

**Note.** Parameters  $K$ ,  $P$ ,  $e$ ,  $\omega$ , and  $M_0$  are the Keplerian parameters: radial velocity amplitude, signal period, eccentricity, argument of periastris, and mean anomaly with respect to epoch  $t = 2,450,000$  JD, respectively. The uncertainty in stellar mass has been accounted for when estimating the minimum mass and semimajor axis corresponding to the signal under planetary interpretation for its origin.

correlation between the HIRES velocities and  $S$ -index with a parameter value of  $1.62$  [0.21, 3.18]  $\text{ms}^{-1}$ , which indicates a  $3.1\sigma$  significance.

We have tabulated the parameters of the radial velocity signal, assuming it has a Keplerian shape, in Table 1, together with the “nuisance parameters” in the statistical model. We also tabulated the estimates when not including the correlations between velocities and the activity indicators in the model—i.e., when fixing parameters  $c_{i,l} = 0$  for all indices and both instruments. We note that the two solutions are not statistically significantly different for the Keplerian parameters. This is demonstrated by the fact that the 99% credibility intervals of the parameters of the signal are not distinct between the two models.<sup>12</sup> This implies that the properties of the signal are independent of whether or not we account for the correlations between the velocities and activity data. However, as discussed above, there is a significant correlation between the HARPS radial velocities and BIS values, and we thus consider the solution that includes the correlations to be more trustworthy (the solution on the left-hand side in Table 1).

### 5.3. Color- and Time-invariance of the Radial Velocity Variations

A true Keplerian Doppler signal of planetary origin cannot depend on the wavelength range of the spectrograph. Although Reiners et al. (2013) tested the wavelength dependence of the signal in the AD Leo velocities by measuring the amplitude of the signal for different subsets of the 72 HARPS orders, they did not account for red noise or correlations between the velocities and activity indicators. We repeated this experiment

<sup>12</sup> This means that when considering the intervals to be Bayesian credibility sets, these sets have an intersection that is not an empty set.

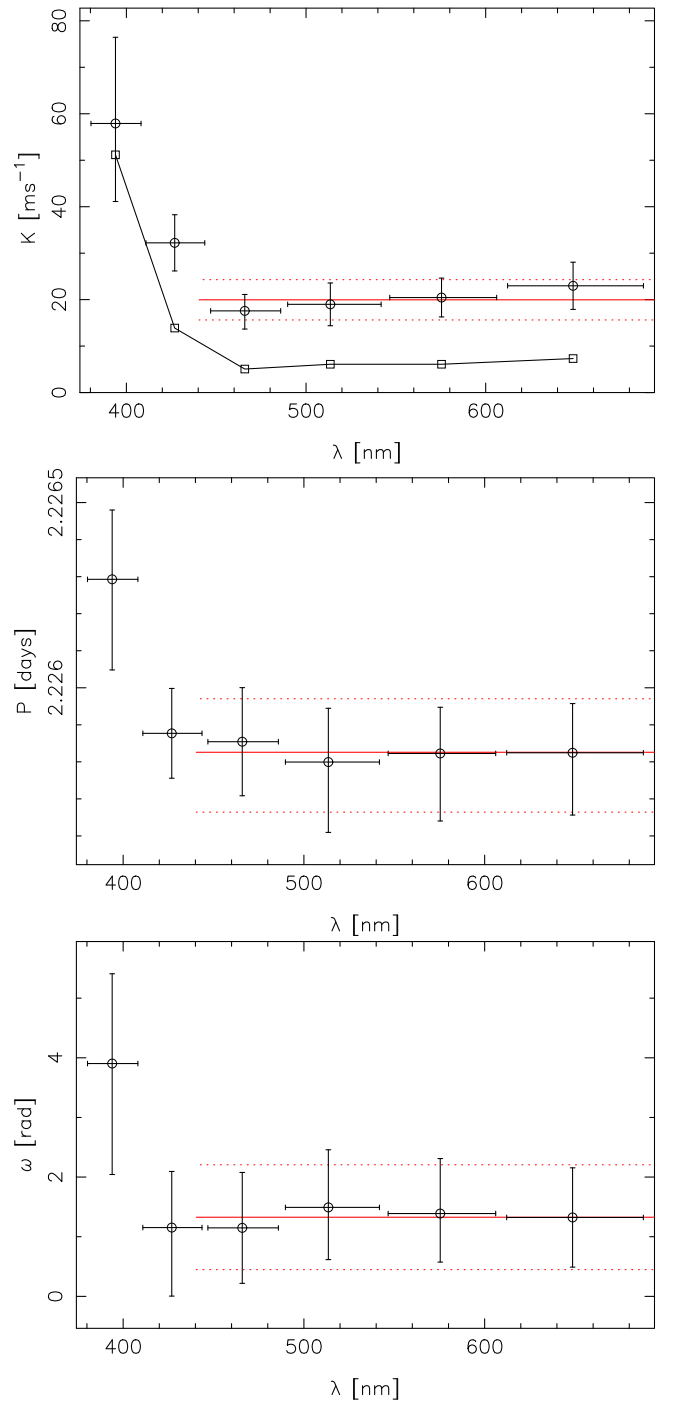


**Figure 8.** Wavelength dependence of the signal in the HARPS radial velocities. Parameter estimates for the velocities are calculated for six sets of 12 HARPS orders: radial velocity amplitude (top panel), signal period (middle panel), and signal phase when assuming a circular solution (bottom panel). The solid (dotted) red horizontal line denotes the estimate (99% credibility interval) obtained for the HARPS-TERRA velocities based on the reddest 50 orders (see Anglada-Escudé & Butler 2012). In the top panel, the squares and black lines denote the data rms for comparison. The horizontal error bars denote the wavelength range of the 12 HARPS orders used to obtain the radial velocities.

by calculating the weighted mean velocities for six sets of 12 orders. Apart from the bluest 24 HARPS orders that were found to be heavily contaminated by activity (see also Anglada-Escudé & Butler 2012), we found the parameters of the signal to be independent of the selected wavelength range. This is demonstrated in Figure 8, where we have plotted the

signal amplitude, period, and phase (when assuming a circular solution) as a function of wavelength. In Table 4, the radial velocities for individual orders are given. The remarkable stability of the signal represents the hallmark of a Keplerian signal of planetary origin and is difficult to interpret as a signal that is caused by starspots corotating on the stellar surface. Although the bluest orders do not appear to agree with the rest of the orders in this respect, we note that the solution for the first 12 orders is actually a highly eccentric solution that arises from the activity-induced variations (and correspondingly higher rms) at the bluest wavelengths.

The standard deviation of the radial velocities from the bluest 12 orders was found to be  $77.89 \text{ ms}^{-1}$ , whereas that of the next bluest 12 orders was  $31.07 \text{ ms}^{-1}$ . This arises due to a combination of lower signal-to-noise and the bluer orders being more prone to activity-induced variability. As a consequence, it was not possible for us to detect the signal correctly in the bluest 12 orders and probably caused biases in the estimated parameters of the signal for the second bluest 12 orders (Figure 8). However, when using the so-called differential velocities of Feng et al. (2017) as activity proxies, we could see the signal as a clear probability maximum at the same period in the period space for all six wavelength ranges. Although independent detection of the signal was only possible for the four redmost sets of 12 HARPS orders, the differential velocities helped remove activity-induced variability such that the signal could be seen throughout the HARPS wavelength range.

Another signpost that a periodic signal in radial velocity is a Keplerian one, caused by a planet orbiting the star, is time invariance. We tested this time invariance by looking more closely at a 60 day period during which HARPS was used to observe AD Leo 28 times: over nine ( $N = 14$ ) and eight ( $N = 8$ ) consecutive nights and then six times over a period of 11 nights. These observations are treated as independent data subsets and plotted in Figure 9, together with the estimated Keplerian curve. As can be seen in Figure 9, over this period of 60 days, the periodic variability is remarkably stable and consistent with a time-invariant signal.

Due to the lack of another period of observations with suitably high observational cadence, we then analyzed in combination the HARPS data not included in the above 60 day period and HIRES data. This combined data set with 19 HARPS and 42 HIRES radial velocities showed evidence for a consistent periodicity with the 60 day HARPS observing run. Assuming zero eccentricity, the signals in the 60 day observing run and the rest of the data have amplitudes of 23.13 [19.28, 26.24] and 18.78 [11.68, 25.87]  $\text{ms}^{-1}$ , periods of 2.22290 [2.21810, 2.22645] and 2.22576 [2.22507, 2.22601] days, and phases of 4.08 [0,  $2\pi$ ] and 1.83 [0.28, 4.81] rad, respectively. Although the solution given the 60 day HARPS observing run is rather uncertain (the former solution above), this demonstrates that the signal is stable, with a precision of almost two orders of magnitude better than what was observed for the photometric rotation signal in the *MOST* data in Section 4.1.

#### 5.4. Simulated Variable Signals

To investigate whether starspots corotating on the stellar surface could produce coherent radial velocity signals over a period of several years, such as the baseline of the radial velocity data of AD Leo of 4733 days, we generated artificial

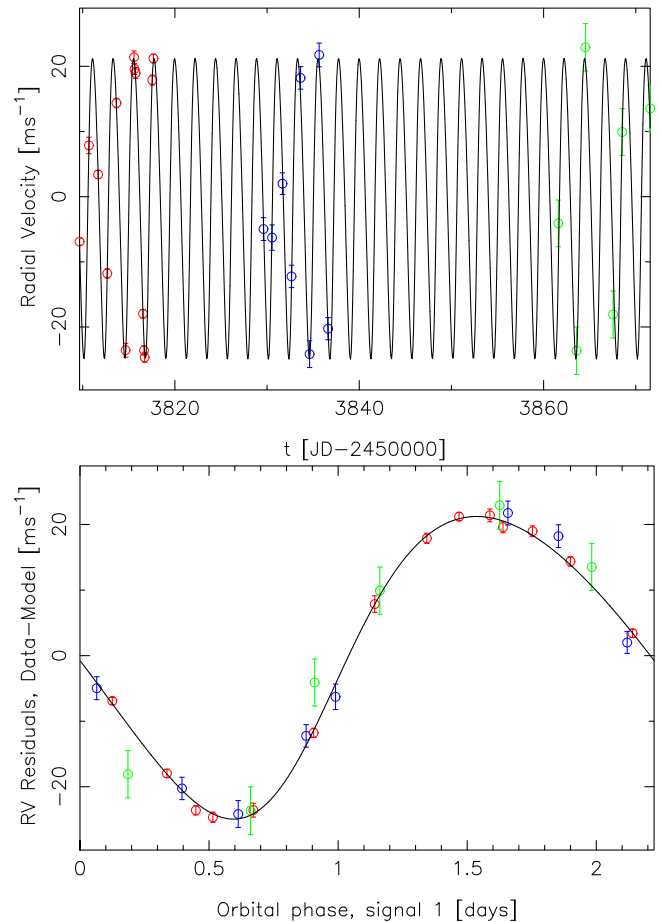


**Figure 9.** HARPS radial velocities of AD Leo between JDs 2453809.7 and 2453871.6 as a function of time (top panel) and folded on the phase of the signal (bottom panel). The black curve denotes the estimated Keplerian curve. The three temporal subsets of data denoted by different colors have been treated as independent data sets with independent nuisance parameters.

radial velocities to study the detectability of evolving signals in the available radial velocity data.

We generated artificial data sets with the same properties as were observed for the HARPS and HIRES data (Table 1) and added one sinusoidal signal in the data with  $P = 2.23$  days and  $K = 20.0 \text{ ms}^{-1}$ . Because the *MOST* photometry indicated that, within a period of 9 days, the photometric signal evolved considerably in phase, period, and amplitude, we changed the phase of the signal by an angle of  $\psi t$ , where  $\psi$  is a constant and  $t$  is time. Parameter  $\psi$  was selected to have values  $\psi \in \frac{1}{10}[0, 1, \dots, 7]$  rad week $^{-1}$ —i.e., the signal was made to vary linearly as a function of time from 0 to 0.7 rad week $^{-1}$ . We denote these data sets as S1, S2, ..., S8, respectively. Although only a toy model, this still enabled us to study the sensitivity of our signal detection to evolving signals. To avoid analyzing the artificial data with the same model as was used to generate it (i.e., committing an “inverse crime”; Kaipio & Somersalo 2005), we used a noise model with third-order moving average terms with second- and third-order components fixed such that  $\phi_2 = 0.3$  and  $\phi_3 = 0.1$ , respectively, whereas we only applied the first-order moving average model when analyzing the data.

The simulated radial velocity data sets were generated such that the injected signal was varied less rapidly than the photometric one in the *MOST* data and did not disappear, contrary to what appears to be the case for the photometric



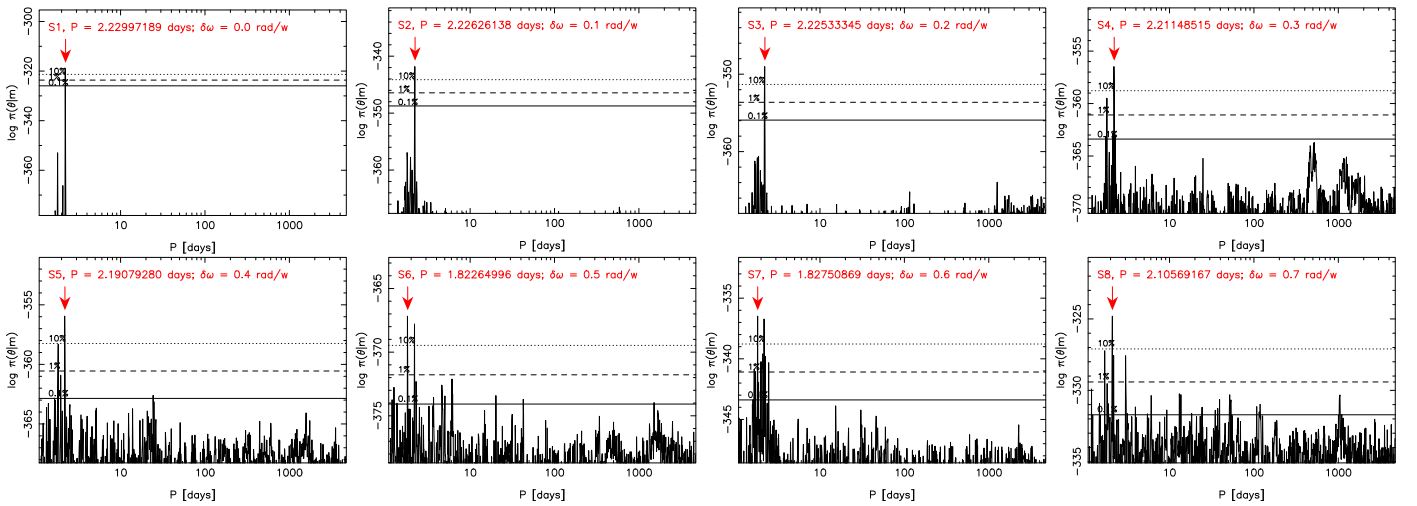


**Figure 10.** Estimated posterior probability densities as functions of signal period for artificial data sets with injected signals. The rate of change in the phase of the signals ( $\delta\omega$ ) is denoted in each panel in  $\text{rad week}^{-1}$ . The red arrows denote the global probability maxima, and the horizontal lines indicate the 10% (dotted), 1% (dashed), and 0.1% (solid) equiprobability thresholds with respect to the maxima.

signal in the ASAS data (Figure 4). Although we expected a slightly variable signal to cause a clear probability maximum due to the concentration of HARPS data on a period of 60 days (Section 5.3), it was also expected that a more rapidly varying signal would make the detection less probable or impossible. This is indeed what happened, as can be seen in Figure 10, where we have plotted the posterior probability densities as functions of signal periods given artificial data sets with signals whose phases evolve. While the signal was very clear for the simulated data set S1 with a stationary signal (Figure 10, top left panel), it was also clearly detected for sets S2 and S3, for which the evolution in the signal phase was 0.1 and 0.2  $\text{rad week}^{-1}$ , respectively. With a more rapidly evolving phase of 0.3  $\text{rad week}^{-1}$ , the signal and its alias became less and less unique (S4), whereas even more rapidly evolving signals could not be detected as unique solutions despite the fact that the posterior densities showed hints of periodicities close to the period of the injected signal and its daily alias (Figure 10, bottom panels).

The stationary signal (S1) corresponds to the only simulated case where the signal was detected as clearly as in the actual HARPS and HIRES radial velocity data. For the simulated set S1, the signal was detected with a logarithm of Bayes factor of 58.77—close to the value obtained for the actual data of 52.25. For sets S2 and S3, this value decreased to 21.24 and 6.51; the latter one is only barely above the detection threshold of 5.01. Together with the fact that the signals lose their uniqueness when the signal varies more than 0.2  $\text{rad week}^{-1}$ , this implies that an evolving signal would be unlikely to cause the observed radial velocity variability. This suggests that only signals that do not vary as a function of time can be detected as strong probability maxima in the AD Leo radial velocity data (Figure 6).

Because a linearly evolving phase is an unrealistic description of the potentially very complex patterns of starspot evolution, we also tested a simple stochastic variability model. When assuming that the phase of the signal was a random variable drawn from a Gaussian probability distribution centered at the current phase and a standard deviation  $\sigma_\psi$  ranging from 0 to 0.7 rad, as was the case for the linearly

evolving  $\psi$  above, we updated the phase randomly after 2–4 rotation periods and again searched for signals in the generated artificial data sets. For such stochastic variability, the signal could not be detected in the data for  $\sigma_\psi > 0.3$  rad. Although detection was possible for a phase changing more slowly than that, our test again suggested that variable signals generally cannot be detected unless the rate of variability is low.

It thus appears that, unlike the photometric signal (Figure 3) that varies in phase, amplitude, and period, the radial velocity signal of AD Leo appears to be caused by a stationary process. At least, it can be said that the signal in AD Leo radial velocities is consistent with a stationary signal.

## 6. AD Leo in the Context of Starspot Observations and Models

We investigated the possibility of obtaining the observed photometric variability on AD Leo by modeling spots using the Doppler Tomography of Stars program (Collier Cameron 2001), which models both spectroscopic and photometric data. We used the model spectra of Baraffe et al. (2015) to obtain spectral contrast ratios for spots with 2900 and 3000 K and a photosphere with 3400 K. In other words, for AD Leo, we assumed spots that are 400 and 500 K cooler than the photosphere, as indicated by Berdyugina (2005) and Barnes et al. (2017).

We tested scenarios for spots with radii of  $5^\circ$ ,  $10^\circ$ , and  $15^\circ$  and fixed the stellar axial inclination at  $15^\circ$ . The results are shown in Figure 11, which shows the photometric amplitude ( $A$ ) as a function of the spectroscopic radial velocity amplitude ( $K$ ) induced by the spots. The points on each curve denote the amplitudes for a spot at latitude  $90^\circ$  (0, 0) and then at successively lower latitudes down to  $30^\circ$  in  $5^\circ$  intervals. For spots with latitude  $<50^\circ$ , the velocity amplitude begins to decrease, while the photometric amplitude decreases slightly for spots at latitude  $<40^\circ$ . This is a consequence of the center-to-limb brightness variation. For a spot radius just larger than  $10^\circ$  and  $T_{\text{phot}} - T_{\text{spot}} = 500$  K, a spot at latitude  $40^\circ$  is required to approximately reproduce the observed amplitude seen in the ASAS-N data and by Spiesman & Hawley (1986).

Only low-latitude spots are able to reproduce both the observed photometric and spectroscopic amplitudes for a star



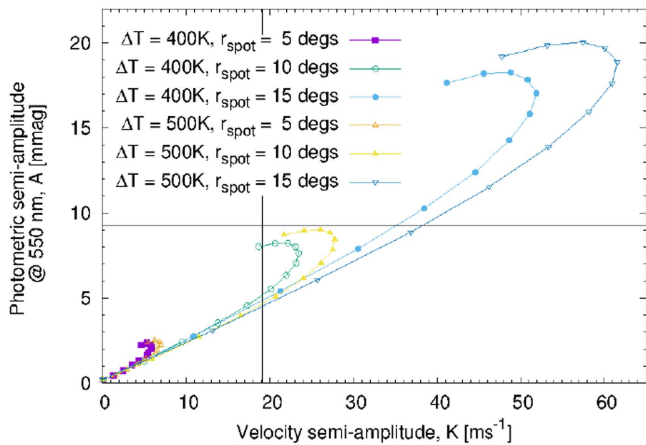


**Figure 11.** Photometric amplitude as a function of radial velocity amplitude for a star with axial inclination  $i = 15^\circ$ . Curves are plotted for spot radii of  $r_{\text{spot}} = 5^\circ, 10^\circ,$  and  $15^\circ$  with spot contrasts of  $T_{\text{phot}} - T_{\text{spot}} = \Delta T = 400$  and  $500$  K. The points defining each curve are for different spot latitudes ranging from  $30^\circ$  to  $90^\circ$  (at 0, 0) in steps of  $5^\circ$ . The observed photometric and spectroscopic amplitudes are denoted by the horizontal and vertical lines, respectively.

with  $i = 15^\circ$ . For the photometric amplitude observed in ASAS-N, larger spots at high latitudes (spot radius of  $15^\circ$  in Figure 11) induce a radial velocity (RV) variation that is much larger than observed. If the photometric amplitude is indeed underestimated (as suggested in Section 4.1) and closer to 12 mas, as reported by Spiesman & Hawley (1986), or more, it becomes even more difficult to explain the radial velocity and photometric signals with starspots. However, the radial velocity observations are not contemporaneous with the photometric observations. If the measured radial velocity amplitude of  $19 \text{ ms}^{-1}$  is due to the reflex motion of a planet, our simulations suggest that when the high-cadence radial velocity observations were taken, the spot-induced photometric rotation amplitude must have been small. This fits well with our findings in Section 4, where the stellar rotation is not always detected in the photometry, implying a significantly smaller starspot.

Realistically, a single spot is probably an oversimplification. Barnes et al. (2015, 2017) showed that rapidly rotating M dwarfs exhibit much smaller spots distributed at various longitudes and latitudes. It thus seems likely that photometric variability on AD Leo is only detectable when enough spots are present, i.e., when spot coverage is increased and the star is thus at its brightness minimum (see Figure 2). As demonstrated by *MOST* photometry (Section 4.1) and the images in Barnes et al. (2017), spots can be stable on timescales of a few days. Beyond that timescale, the stability of individual spots or spot groups is rather poorly constrained. The Barnes et al. (2017) observations for GJ 791.2A (M4.5) separated by a year demonstrate a significant change in the distribution of spots at low and intermediate latitudes and that polar and circumpolar spot structures are changing significantly. Although these are rather limited observational constraints, these results do not appear to support the interpretation that long-lived spots could exist for long enough to induce a stable RV signal.

## 7. Comparison to Other M Dwarfs

### 7.1. Rapid Rotators

The ASAS survey has been used to identify several nearby M dwarfs with short ( $< 10$  days) photometric rotation periods

**Table 2**

List of M Dwarfs Included in the HARPS, HIRES, and/or PFS Radial Velocity Surveys for Which Photometric Rotation Periods with  $P < 10$  Days Are Known Based on ASAS-S Photometry

Target	$P_{\text{rot}}$ (days)	$A$ (mmag)	$N$	$\sigma(v)$ ( $\text{ms}^{-1}$ )
GJ 182	4.37	28.21	9	217.1
GJ 285	2.78	20.61	30	84.7
GJ 408	3.55	8.06	68	5.5
GJ 494	2.89	13.54	2	...
GJ 729	2.87	9.20	97	23.9
GJ 803	4.86	16.35	35	136.6
GJ 841A	1.12	10.77	6	...
GJ 1264	6.66	16.10	1	...
GJ 1267	1.61	4.46	39	5.0
HIP 31878	9.15	11.19	26	40.1

**Note.** Here  $A$  denotes the amplitude of the photometric signal and  $N$  and  $\sigma(v)$  denote the number of radial velocity data available for the target and the standard deviation of the velocities, respectively.

(Kiraga & Stepien 2007). We identified 10 targets in a sample of 360 nearby M dwarfs (Tuomi et al. 2018) for which the ASAS-S photometry shows evidence for periodicities shorter than 10 days (Table 2). We have tabulated the corresponding significant (exceeding 0.1% FAP) photometric periodicities with  $P_{\text{rot}} < 10$  days in Table 2 and interpret them as photometric rotation periods of the stars with period  $P_{\text{rot}}$ . We have also plotted the likelihood ratio periodograms of these targets in Figure 12 to visually demonstrate the significance of the detected photometric rotation periods. All these targets have also been observed spectroscopically with HARPS, HIRES, and/or the Planet Finding Spectrograph (PFS), and we thus examined the radial velocity data sets in order to search for counterparts of the photometric periodicities.

We also investigated whether the available radial velocities of the targets in Table 2 showed evidence for signals that could be interpreted as counterparts of the photometric rotation periods. Apart from GJ 494 and GJ 1264 that only had two and one radial velocity measurements available, respectively, and GJ 841A, whose HARPS spectra were contaminated and resulted in radial velocities varying at a  $10 \text{ km s}^{-1}$  level, we searched for such counterparts of photometric rotation periods with posterior samplings. The resulting estimated posterior densities as functions of signal periods are shown in Figure 13. We also show the posterior given AD Leo (GJ 388) data for the same period space between 1 and 12 days.

It can be seen in Figure 13 that only AD Leo (GJ 388; left column, second panel) shows evidence for a unique radial velocity signal in the sense that there are no local maxima exceeding the 0.1% equiprobability threshold of the global maximum. However, there seems to be a reasonable correspondence in the sense that all targets have global posterior maxima at or near the detected photometric periodicities, even though the maxima in the radial velocities are far from unique (Figure 13). It is thus likely that the radial velocities contain periodic variabilities corresponding to the photometric rotation periods. But AD Leo is the exception in this sense, as it is the only one with a unique short-period radial velocity signal.

We interpret this as an indication that such rapidly rotating M dwarfs do not readily produce clearly distinguishable radial velocity signals at or near the rotation period. This is the case

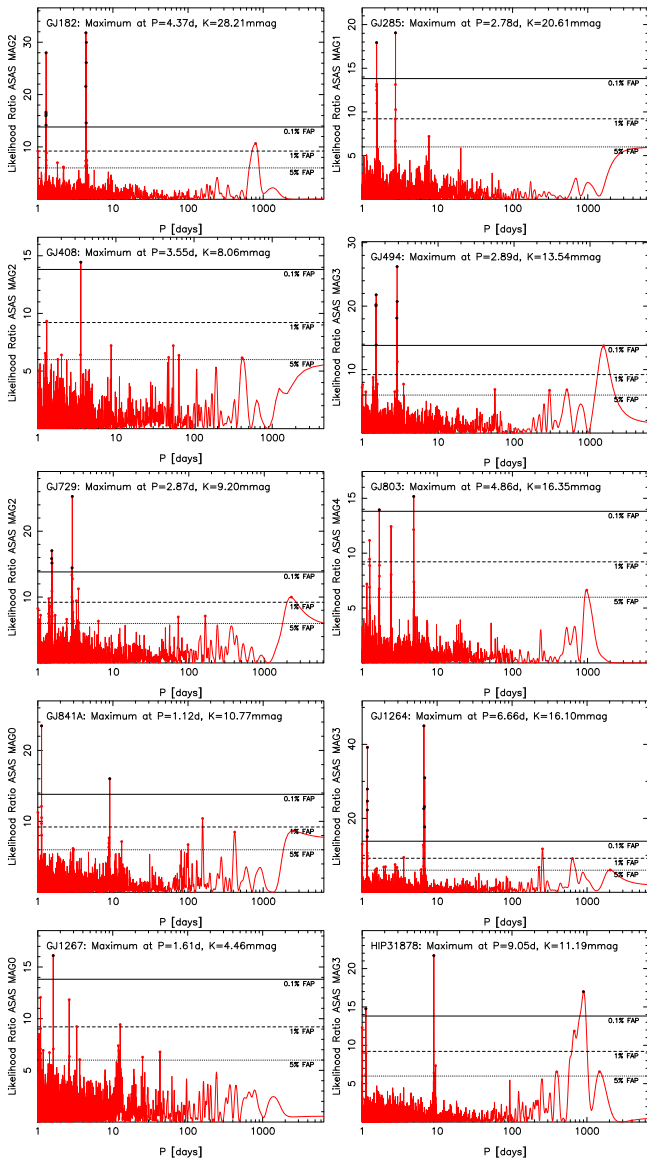


**Figure 12.** Logarithm of the likelihood ratio periodogram of the Grade A ASAS-S photometry, with  $5\sigma$  outliers removed for selected nearby M dwarfs for which there is evidence for a photometric rotation period with  $P_{\text{rot}} < 10$  days.

even when the photometric rotation period is readily detectable with ASAS photometry. When searching for signals in the data of the comparison stars (Figure 13), we obtain broadly similar results as those for our artificial data sets with evolving signals (Figure 10); i.e., there are no unique and significant probability maxima. AD Leo clearly represents an exception in both these respects.

It was not possible to study the dependence of the comparison target radial velocity signals on spectral wavelength, as was done for AD Leo (Figure 8). We calculated the radial velocities for the six wavelength intervals, each corresponding to 12 HARPS orders, for GJ 803 that had the most HARPS observations available ( $N = 20$  after removing outliers). Significant periodicities could not be detected in any of these six sets, and we thus could not study the wavelength dependence of signals caused by purely stellar rotation. However, the probability maximum corresponded to different

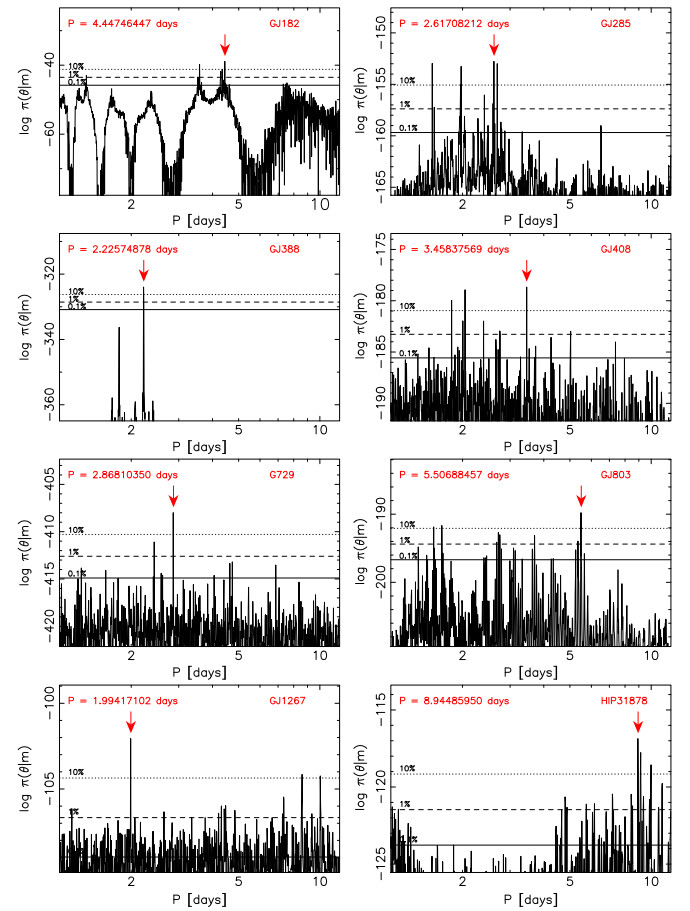


**Figure 13.** Estimated posterior probability density as a function of the period of the signal. The horizontal lines denote the 10% (dotted), 1% (dashed), and 0.1% (solid) equiprobability thresholds with respect to the maximum denoted by the red arrows.

periods in each of the six wavelength intervals. These periods ranged from 2.8 to 6.3 days, but it remains uncertain whether any of them actually correspond to the photometric rotation period of the star of 4.86 days.

## 7.2. The Slowly Rotating Planet Host GJ 674

Finally, we analyzed the HARPS radial velocity data (see Tables 5 and 6) of GJ 674, a quiescent slowly rotating M dwarf that has been reported to be a host to a candidate planet with a minimum mass of  $11.09 M_{\oplus}$  with an orbital period of  $4.6938 \pm 0.007$  days (Bonfils et al. 2007). Moreover, as discussed by Bonfils et al. (2007) and Suárez Mascareño et al. (2015), the HARPS radial velocities of GJ 674 also show evidence for the star's rotation period. This period was estimated to be  $34.8467 \pm 0.0324$  days by Bonfils et al. (2007), but other authors provide slightly different estimates of  $32.9 \pm 0.1$  days (Suárez Mascareño et al. 2015) based on spectroscopic activity indices and 33.29 days (Kiraga & Stepien 2007) based on ASAS photometry. Because this target provides an ideal test case for studying the differences between planet- and rotation-induced signals, we examined the wavelength dependence of the two signals based on radial velocity data calculated for different wavelength ranges, as we did for AD Leo in Section 5.3.

As is expected for a planetary signal, the signal of GJ 674b was consistently detected in all but the bluest 12 HARPS

**Table 3**  
HARPS Data of AD Leo

$t$ [JD-2450000]	$v$ (ms $^{-1}$ )	$\sigma_v$ (ms $^{-1}$ )	BIS (ms $^{-1}$ )	FWHM (ms $^{-1}$ )	$S$ (ms $^{-1}$ )
2452986.8579	27.05	1.86	-15.03	3521.66	8.208
2453511.5468	-15.67	1.15	-10.57	3527.78	8.891
2453520.5205	-13.86	1.06	-6.66	3524.64	8.232
2453543.4808	15.27	1.14	-6.62	3530.43	6.919
2453544.4518	-6.06	0.86	-6.23	3534.29	7.811
2453550.4596	41.73	2.07	-14.23	3522.10	7.026
2453728.8648	38.93	1.36	-10.10	3525.78	10.308
2453758.7540	-18.71	0.88	-8.21	3523.30	7.151
2453760.7547	-9.90	0.81	-6.21	3533.71	8.565
2453761.7800	19.20	0.83	-10.04	3520.08	7.369
2453783.7255	-4.53	0.71	-6.76	3524.50	7.576
2453785.7264	-15.76	0.86	-9.08	3529.40	6.955
2453809.6599	0.00	0.52	-9.49	3525.41	7.037
2453810.6767	13.63	1.26	-8.86	3514.12	11.415
2453811.6750	9.90	0.62	-12.42	3529.17	8.512
2453812.6637	-5.84	0.71	-9.97	3514.26	8.135
2453813.6584	22.38	0.73	-5.76	3532.84	7.916
2453814.6540	-16.21	1.06	-6.89	3525.54	6.941
2453815.5702	26.82	0.97	-16.25	3522.02	7.188
2453815.6211	26.18	0.85	-11.89	3527.75	7.324
2453815.7354	25.17	0.82	-10.47	3516.77	7.135
2453816.5433	-11.46	0.62	-9.59	3521.54	7.795
2453816.6552	-16.34	0.71	-6.39	3522.61	7.150
2453816.7211	-17.59	0.78	-6.83	3519.82	7.263
2453817.5500	24.85	0.77	-8.59	3523.99	7.423
2453817.6749	27.92	0.66	-10.12	3525.81	8.399
2453829.6146	0.88	0.77	-9.81	3520.37	7.688
2453830.5397	-4.17	1.14	-9.00	3504.41	9.871
2453831.6694	10.38	0.55	-12.54	3521.13	6.977
2453832.6497	-8.13	0.69	-5.59	3511.21	7.954
2453833.6269	24.45	0.72	-11.10	3523.54	7.195
2453834.6103	-23.28	1.33	-4.47	3517.78	9.454
2453835.6551	28.84	0.91	-12.59	3518.32	7.368
2453836.6165	-15.98	0.65	-3.33	3524.45	6.811
2453861.5934	1.93	0.70	-9.12	3502.93	7.065
2453863.5687	-17.61	0.93	-6.54	3519.25	8.321
2453864.5340	30.04	0.93	-13.78	3517.17	7.522
2453867.5417	-10.17	0.76	-7.56	3514.19	7.097
2453868.5177	22.94	0.71	-12.73	3517.50	7.330
2453871.5622	19.51	0.62	-8.47	3517.11	7.414
2456656.8493	-31.74	1.16	-0.98	3542.60	7.184
2456656.8602	-28.41	1.03	-3.16	3539.87	7.314
2456657.8522	40.05	1.28	-18.92	3544.42	8.095
2456658.8644	-38.27	0.87	-0.27	3547.32	7.422
2456658.8755	-38.61	1.52	0.29	3547.48	7.426
2456659.8581	42.94	1.58	-15.30	3539.94	7.658
2456797.5118	-24.02	0.74	-1.73	3541.87	8.375

orders. For the five reddest sets of 12 orders, we obtained a consistent periodicity of  $4.6950 \pm 0.0002$  days and an amplitude of  $8.7 \pm 0.3$  ms $^{-1}$  that also agrees very well with the solution reported by Bonfils et al. (2007).

However, the rotation-induced radial velocity signal of GJ 674 was found to be dependent on wavelength. The rotation signal could not be detected in the two bluest sets of 12 orders, 1–12 and 13–24, at all, although the latter showed hints of a periodicity of 36.67 days corresponding to the highest probability maximum in the period space. In radial velocities calculated for orders 25–36, 37–48, 49–60, and 61–72, we detected periodicities of  $36.66 \pm 0.19$ ,  $3.6708 \pm 0.0004$ ,  $36.18 \pm 0.05$ , and  $33.33 \pm 0.03$ , respectively, although the last set of orders had two roughly equally high probability maxima with an alternative solution at a period of

$36.66 \pm 0.03$  days (Figure 14). According to these results, the rotation-induced signal is not found consistently at the same period but varies as a function of wavelength. Moreover, a signal corresponding to the star’s rotation period could not be identified in the radial velocities calculated for orders 37–48, but another signal near 4 days was present instead. This signal was also present in orders 49–60 as a secondary solution (Figure 14, bottom left panel). We did not observe significant differences in the amplitudes of the signals as a function of wavelength because the amplitude of the rotation-induced signal had an amplitude below 3 ms $^{-1}$  with uncertainties of roughly 1 ms $^{-1}$ , making the available precision insufficient for determining possible differences in amplitude as a function of wavelength. These results demonstrate that stellar rotation does not readily produce wavelength-invariant radial velocity signals

**Table 4**  
Example of HARPS Radial Velocity of AD Leo for All 72 Individual Orders  $v_i$ ,  $i = 1, \dots, 72$

$t$ [JD-2450000]	$v_1$ (ms $^{-1}$ )	$\sigma_{v_1}$ (ms $^{-1}$ )	$v_2$ (ms $^{-1}$ )	$\sigma_{v_2}$ (ms $^{-1}$ )	$v_3$ (ms $^{-1}$ )	$\sigma_{v_3}$ (ms $^{-1}$ )
2986.8579	502.80	300.23	-1153.97	276.03	190.56	289.89
3511.5468	-38.00	141.87	-94.04	133.81	521.06	126.51
3520.5205	158.29	191.61	471.33	187.46	278.08	169.40
3543.4808	138.40	240.76	17.90	227.65	-75.73	216.12
3544.4518	-377.68	171.55	-354.19	162.54	-156.08	148.84
3550.4596	1176.80	321.81	-744.10	286.01	369.98	296.29
3728.8648	-8.87	162.99	195.14	155.38	-16.01	144.67
3758.7540	81.83	129.82	50.39	127.00	-21.92	111.59
3760.7547	-18.18	120.27	-472.43	116.04	168.59	107.86
3761.7800	184.64	107.38	19.01	103.78	-113.55	90.69
3783.7255	-158.69	113.05	103.10	112.32	150.24	96.51
3785.7264	-1.90	111.54	-155.30	115.46	257.99	99.78
3809.6599	49.90	79.20	-143.19	82.32	24.83	69.91
3810.6767	314.57	108.86	296.13	96.35	110.75	84.68
3811.6750	123.42	98.04	200.36	93.21	-131.53	81.88
3812.6637	-157.04	166.80	538.03	159.24	-261.14	145.15
3813.6584	231.57	89.82	-45.62	88.21	-17.41	78.00
3814.6540	-91.03	152.77	-217.45	148.51	-72.68	132.42
3815.5702	-14.76	121.71	232.38	119.64	-153.38	107.72
3815.6211	-217.01	103.38	-41.35	100.24	-227.38	88.13
3815.7354	-400.83	109.28	5.05	105.98	-46.12	90.78
3816.5433	35.14	127.58	194.62	123.77	-150.30	111.89
3816.6552	-186.00	107.40	-201.14	109.34	-39.90	92.84
3816.7211	127.14	116.73	65.59	118.16	-218.59	100.93
3817.5500	154.66	94.25	-95.49	95.87	-76.58	81.27
3817.6749	84.06	103.83	83.03	99.67	100.74	88.41
3829.6146	-247.02	97.13	76.68	95.42	118.33	81.55
3830.5397	164.12	119.88	-63.25	112.66	-100.52	101.58
3831.6694	224.15	89.65	-165.35	91.34	177.34	76.56
3832.6497	124.92	92.06	-128.90	95.22	-233.24	82.47
3833.6269	-130.12	79.78	25.88	76.59	65.00	66.56
3834.6103	-208.36	85.12	-248.17	79.18	99.07	68.95
3835.6551	-73.31	98.09	-53.44	95.03	-223.53	84.78
3836.6165	-166.97	87.31	118.87	87.04	-320.86	75.65
3861.5934	629.82	127.62	106.85	126.00	-329.65	110.16
3863.5687	-70.57	103.04	-450.80	96.21	76.85	85.86
3864.5340	25.72	106.61	156.79	108.93	147.68	92.01
3867.5417	-415.38	118.93	107.27	115.52	-124.68	101.36
3868.5177	108.62	115.43	-265.25	112.28	-256.27	98.14
3871.5622	-94.14	105.93	-71.85	104.76	118.22	92.04
6656.8493	291.80	204.95	-289.60	194.67	142.49	175.07
6656.8602	247.43	200.15	-233.94	189.16	542.26	168.08
6657.8522	-208.53	212.18	534.53	194.33	278.32	173.81
6658.8644	-313.55	204.48	-212.75	197.12	-231.53	169.65
6658.8755	-42.68	197.72	117.97	189.36	-112.47	162.47
6659.8581	-465.41	291.66	1210.13	257.40	-2.09	247.89
6797.5118	126.76	105.52	271.71	102.69	216.04	90.55

and that the signal observed in AD Leo radial velocities is thus likely caused by a planet orbiting the star.

We further highlight the wavelength dependence and independence of the Keplerian signal in GJ 674 data and the rotation-induced signal near 37 days in Figure 15. We note that the estimated second period is not shown for orders 37–48 in the bottom panel of Figure 15 because there are no significant signals at or near the stellar rotation period and the corresponding second signal for these orders has a period of 3.67 days.

## 8. Discussion

We have presented analyses of ASAS V-band photometry, *MOST* photometry, and HARPS and HIRES radial velocities of

AD Leo. Although AD Leo is a rapidly rotating star with a rotation period of approximately 2.23 days (see Spiesman & Hawley 1986; Morin et al. 2008; Hunt-Walker et al. 2012; Bonfils et al. 2013; Reiners et al. 2013, and the current work), we only see evidence for a photometric rotation period of the star in ASAS-N and *MOST* photometry (Figure 4) when the star is at a brightness minimum of its activity cycle. This might be due to the brightness minimum corresponding to greater starspot coverage, making the photometric rotation period more visible in the data. Nondetection of this signal in the ASAS-S photometry might indicate that there are not enough spots on the stellar surface or that they are too variable during the brightness maximum to determine the photometric rotation period.



**Table 5**  
Example of HARPS Data of GJ 674

$t$ [JD-2450000]	$v$ (ms <sup>-1</sup> )	$\sigma_v$ (ms <sup>-1</sup> )	BIS (ms <sup>-1</sup> )	FWHM (ms <sup>-1</sup> )	$S$ (ms <sup>-1</sup> )
2453158.7520	9.73	0.73	-8.99	3018.96	1.318
2453205.5995	8.41	0.32	-6.72	3065.91	1.665
2453237.5635	7.53	0.83	-9.55	3070.47	1.382
2453520.7932	3.66	0.54	-8.49	3065.37	1.611
2453580.5685	7.06	0.41	-8.13	3068.93	1.528
2453813.8477	-10.69	0.45	-8.55	3063.31	1.130
2453816.8691	-1.00	0.49	-6.33	3059.31	1.086
2453861.8085	4.73	0.47	-10.11	3064.74	1.204
2453862.7863	10.41	0.38	-7.77	3066.12	1.563
2453863.8105	6.07	0.54	-8.92	3066.16	1.254
2453864.7669	-8.34	0.47	-7.75	3069.48	1.432
2453865.8114	-0.96	0.48	-10.58	3070.48	1.353
2453866.7558	4.98	0.37	-8.74	3071.30	1.755
2453867.8481	6.56	0.44	-8.07	3069.35	1.461
2453868.8393	-4.07	0.43	-5.99	3075.55	1.662
2453869.8038	-11.75	0.49	-8.93	3080.39	2.052
2453870.7388	-3.83	0.65	-9.05	3079.69	1.651
2453871.8606	1.96	0.52	-7.08	3076.56	1.379
2453882.7445	-4.55	0.44	-7.59	3062.54	1.184
2453886.7489	2.98	0.44	-8.69	3063.01	1.081
2453887.7915	-7.14	0.37	-7.69	3060.73	1.006
2453917.7229	-3.22	0.47	-7.40	3058.93	1.121
2453919.7271	5.47	0.66	-4.99	3063.84	1.014
2453921.6271	-8.82	0.39	-8.70	3059.50	1.091
2453944.5860	-13.05	0.66	-6.79	3072.41	1.529
2453947.5906	8.07	1.34	-8.24	3076.75	1.304
2453950.6474	-3.86	0.49	-8.61	3064.41	1.285
2453976.5244	-2.45	0.46	-8.58	3074.71	1.410
2453980.5691	-0.09	0.56	-8.55	3075.49	1.265
2453981.5927	-11.94	0.53	-6.96	3058.65	1.383
2453982.6162	-16.16	0.55	-7.27	3058.62	1.267
2453983.5287	-5.36	0.66	-8.48	3061.14	1.068
2454167.8783	2.75	0.45	-7.76	3073.49	1.336
2454169.8879	-13.41	0.44	-7.93	3072.81	1.410
2454171.8966	1.79	0.46	-6.72	3069.83	1.271
2454173.8674	-1.82	0.41	-8.59	3069.64	1.297
2454340.6256	-0.18	0.39	-9.31	3070.89	1.330
2454342.5927	3.43	0.52	-7.58	3070.21	1.353
2454347.5335	-5.20	0.62	-7.29	3066.48	1.237
2454349.6053	-9.33	0.51	-7.85	3055.05	1.150
2454388.4992	3.41	0.61	-5.06	3057.18	1.579
2454589.8983	-0.64	0.47	-7.35	3060.15	1.347
2454666.7202	0.52	0.55	-7.10	3070.37	1.236
2454732.4793	2.08	0.50	-5.70	3070.98	1.225
2455784.6229	-8.18	0.48	-7.99	3075.52	1.371
2455810.5101	4.61	0.57	-9.67	3078.15	1.306
2455815.5504	6.23	0.55	-9.09	3072.08	1.562
2455817.5325	-7.73	0.62	-7.03	3077.42	2.293
2456385.7728	-7.98	0.71	-8.95	3074.62	1.184
2456386.7932	-3.14	0.75	-11.37	3069.91	1.241
2456387.8161	2.25	0.63	-9.86	3069.89	1.332
2456388.7910	7.12	0.57	-10.29	3072.57	1.399
2456389.7575	3.71	0.69	-9.42	3071.48	1.473
2456390.7806	-9.38	0.85	-8.71	3074.05	1.581
2456393.8390	11.11	0.99	-7.01	3084.10	1.375
2456394.8345	-1.66	0.80	-11.96	3080.26	1.331
2456395.7581	-7.81	0.69	-8.00	3078.12	1.435
2456396.8055	-0.72	0.67	-10.36	3080.82	1.562
2456397.8548	5.22	0.70	-8.32	3083.16	1.321
2456398.7295	3.48	0.77	-8.76	3079.93	1.463
2456399.7167	-7.72	0.68	-7.01	3090.04	1.446
2456400.7247	-8.25	0.63	-7.45	3077.71	1.498
2456401.7452	0.00	0.70	-10.21	3080.23	1.647
2456402.7721	4.74	0.80	-7.25	3084.09	1.617

**Table 6**  
Example of HARPS Radial Velocity of GJ 674 for All 72 Individual Orders  $v_i$ ,  $i = 1, \dots, 72$

$t$ [JD-2450000]	$v_1$ (ms <sup>-1</sup> )	$\sigma_{v_1}$ (ms <sup>-1</sup> )	$v_2$ (ms <sup>-1</sup> )	$\sigma_{v_2}$ (ms <sup>-1</sup> )	$v_3$ (ms <sup>-1</sup> )	$\sigma_{v_3}$ (ms <sup>-1</sup> )
3158.7520	-588.71	263.81	227.27	269.05	1749.74	276.26
3205.5995	12.31	101.82	-47.32	116.04	15.93	90.61
3237.5635	39.12	214.44	-1319.67	226.17	-159.88	200.46
3520.7932	-134.69	121.59	-183.98	138.57	-28.22	105.64
3580.5685	-2.02	89.88	0.17	101.79	-39.91	82.02
3813.8477	-57.20	58.22	-117.54	69.24	35.22	50.26
3816.8691	-166.60	65.66	168.84	77.43	-20.63	58.47
3861.8085	111.50	66.70	-93.26	75.73	25.76	57.69
3862.7863	-41.33	81.56	194.86	92.34	50.25	72.07
3863.8105	16.53	72.25	34.94	82.14	93.66	64.76
3864.7669	190.33	73.11	20.47	83.28	-112.01	65.66
3865.8114	-97.21	63.40	-91.95	74.01	31.54	54.87
3866.7558	70.73	55.05	106.57	61.28	15.81	47.47
3867.8481	3.60	82.11	-120.05	87.68	-36.68	66.88
3868.8393	-32.43	68.11	-25.00	75.97	-88.54	60.51
3869.8038	22.40	71.35	135.15	79.57	-183.62	60.78
3870.7388	-225.05	102.91	-48.89	112.87	93.43	90.79
3871.8606	84.78	75.72	272.50	84.60	0.74	64.68
3882.7445	-142.07	55.19	-6.12	63.29	-1.25	47.93
3886.7489	54.69	51.51	-34.08	58.77	-38.51	44.38
3887.7915	41.26	54.68	-69.51	62.46	43.17	47.53
3917.7229	-67.53	102.54	-307.72	113.21	-164.23	88.00
3919.7271	266.24	139.73	138.67	153.85	118.44	121.60
3921.6271	55.45	55.68	-133.81	65.64	-50.26	51.47
3944.5860	-116.93	111.85	-169.81	119.60	-102.59	102.00
3947.5906	-419.66	215.97	-574.18	224.53	-506.57	208.66
3950.6474	-22.58	87.82	264.96	98.07	-43.89	77.73
3976.5244	36.70	65.73	-172.51	71.14	8.10	55.64
3980.5691	-66.00	120.14	-104.77	130.93	-49.01	104.40
3981.5927	-24.58	86.43	-118.72	96.98	-119.14	76.33
3982.6162	-150.55	85.05	-208.65	97.15	50.91	76.92
3983.5287	-394.07	119.96	387.17	132.16	219.03	103.19
4167.8783	47.99	71.05	89.18	83.42	29.21	64.07
4169.8879	266.39	66.32	73.14	73.76	-145.35	56.81
4171.8966	13.84	64.57	-41.04	77.54	22.22	57.44
4173.8674	-139.35	71.71	-51.11	83.35	-22.61	63.72
4340.6256	-86.51	64.88	156.99	72.66	31.53	56.34
4342.5927	-168.33	84.39	76.99	92.49	-22.83	77.75
4347.5335	-43.39	87.77	-237.71	100.36	6.53	79.37
4349.6053	-288.70	105.74	-242.57	114.94	-88.61	92.15
4388.4992	410.95	131.62	-165.98	142.65	-372.56	113.86
4589.8983	52.11	70.05	-91.71	82.61	193.71	63.27
4666.7202	159.42	107.67	117.36	118.26	-19.54	96.35
4732.4793	172.13	103.85	-16.30	116.38	-135.62	89.29
5784.6229	106.28	140.50	89.25	151.05	-55.52	118.74
5810.5101	-43.88	111.11	-64.36	118.18	268.38	95.76
5815.5504	-416.05	127.38	-204.83	140.64	24.47	107.59
5817.5325	-371.97	129.16	-368.98	128.88	-296.97	108.19
6385.7728	-26.32	123.76	26.87	144.05	109.07	117.45
6386.7932	-116.45	165.94	-427.02	173.78	247.43	151.03
6387.8161	382.30	139.11	-481.63	149.42	207.95	115.49
6388.7910	31.58	142.91	-389.56	155.37	206.52	125.34
6389.7575	121.32	162.90	-384.28	171.63	-52.14	142.02
6390.7806	-53.28	184.35	-725.17	188.55	101.97	164.66
6393.8390	-569.83	175.81	-1284.30	181.88	-152.91	156.36
6394.8345	-35.35	145.96	-726.20	161.48	137.19	126.25
6395.7581	-118.25	141.99	-1190.94	151.95	-266.51	124.99
6396.8055	0.45	151.23	-983.89	160.24	-98.54	130.24
6397.8548	761.62	154.42	-1555.73	160.96	-347.23	132.46
6398.7295	683.26	154.21	-328.82	167.12	-239.14	137.56
6399.7167	145.08	133.42	-315.28	147.14	101.25	112.60
6400.7247	669.04	166.52	-1103.21	179.43	-567.21	146.99
6401.7452	-120.21	150.96	-737.78	162.96	-631.43	129.01
6402.7721	326.55	179.47	-1694.13	186.14	-375.28	159.66

**Table 7**  
Example of ASAS-N Photometry of AD Leo

$t$ [JD]	V (mag)
2454049.14	9296
2454057.14	9277
2454060.09	9284
2454067.12	9285
2454076.03	9301
2454082.14	9245
2454084.15	9286
2454089.10	9283
2454093.07	9307
2454096.05	9293
2454100.01	9289
2454102.03	9269
2454137.00	9272
2454138.93	9284
2454144.14	9261
2454146.06	9271
2454148.06	9284
2454156.90	9283
2454158.01	9276
2454163.96	9292
2454166.87	9276
2454180.96	9281
2454182.85	9291
2454184.01	9300
2454196.87	9252
2454198.87	9290
2454199.85	9282
2454200.87	9287
2454202.87	9292
2454208.87	9288
2454210.85	9276
2454211.91	9290
2454212.86	9285
2454218.86	9295
2454220.90	9292
2454220.91	9324
2454222.87	9292
2454224.87	9291
2454227.84	9303
2454230.84	9271
2454233.84	9286
2454235.83	9262
2454237.84	9271
2454239.80	9282
2454274.77	9297
2454474.00	9282
2454477.05	9292
2454477.05	9299
2454478.98	9300
2454523.96	9273
2454524.00	9279
2454524.00	9274
2454526.01	9281
2454530.97	9274
2454559.85	9289
2454559.85	9271
2454561.85	9284
2454561.85	9282
2454563.97	9268
2454582.89	9260
2454582.90	9255
2454589.84	9263
2454589.87	9295
2454591.86	9248

**Table 8**  
Example of ASAS-S Photometry of AD Leo

$t$ [JD]	V (mag)
2452622.83	9370
2452625.83	9347
2452628.84	9362
2452628.84	9356
2452635.79	9342
2452635.79	9329
2452637.85	9353
2452643.80	9351
2452645.82	9369
2452649.78	9324
2452651.77	9342
2452657.77	9346
2452661.79	9365
2452663.78	9359
2452665.77	9357
2452667.77	9343
2452669.78	9391
2452671.76	9377
2452673.76	9341
2452673.76	9335
2452675.74	9343
2452677.73	9368
2452681.71	9358
2452683.71	9365
2452690.70	9336
2452691.81	9356
2452694.66	9355
2452695.71	9342
2452696.69	9357
2452698.68	9363
2452700.68	9366
2452702.67	9372
2452704.67	9386
2452706.66	9354
2452710.64	9371
2452712.62	9361
2452717.61	9332
2452719.68	9366
2452723.63	9364
2452725.63	9366
2452727.62	9350
2452729.62	9367
2452733.61	9360
2452735.60	9337
2452737.59	9354
2452743.57	9375
2452745.57	9299
2452751.54	9382
2452754.54	9361
2452764.53	9360
2452776.55	9348
2452784.49	9357
2452786.49	9346
2452789.48	9372
2452811.46	9351
2452813.47	9371
2452975.84	9349
2452976.85	9324
2452978.85	9337
2452982.83	9357
2452994.82	9354
2452997.83	9348
2453005.79	9348
2453007.82	9338

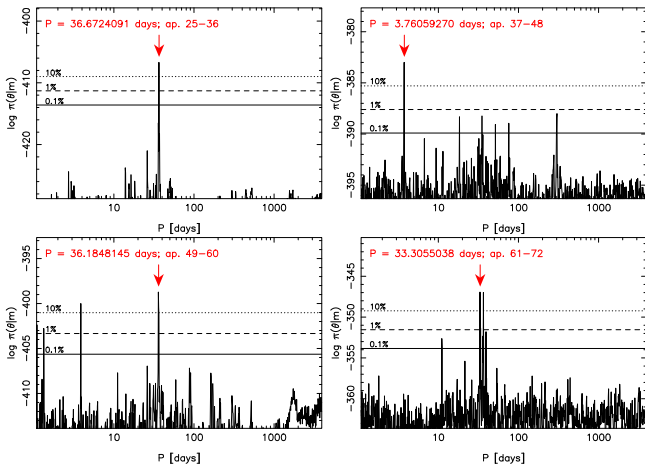


**Figure 14.** Estimated posterior probability densities used to determine the global maxima corresponding to the rotation period in the HARPS radial velocities of GJ 674. The signal of GJ 674b has been accounted for, and the red arrows indicate the positions of the most prominent secondary maxima. The aperture ranges correspond to the four redmost sets of 12 HARPS orders.

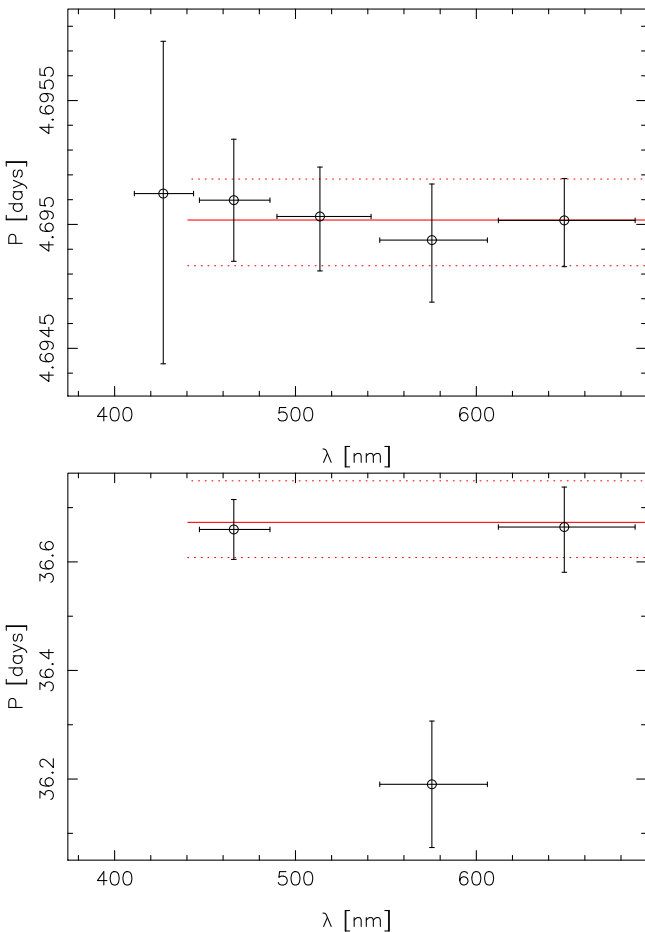


**Figure 15.** Same as Figure 8 but for the period parameters of GJ 674 signals corresponding to planet candidate GJ 674b (top panel) and the rotation-induced signal (bottom panel).

The radial velocities of AD Leo contain a unique and highly significant signal that appears to be time- and wavelength-invariant at a period of  $2.22567 [2.22556, 2.22593]$  days (Figure 6), coinciding with the rotation period of the star. Our results indicate

that the radial velocity signal of AD Leo is independent of the spectral wavelength range (Figure 8) and also time invariant, making it unlikely to have been caused by stellar activity and starspots corotating on the stellar surface. Our tests with simulated data indicate that only stationary periodic processes can give rise to such a clear radial velocity signal as we observed in the HARPS and HIRES radial velocities (Figure 10).

We consider it difficult to interpret stellar rotation as the origin of the time- and wavelength-invariant radial velocity signal. The photometric signal varies much more on short timescales (Section 4.1) than the radial velocity signal appears to do over a baseline of thousands of days (Section 5.3). Our modeling also demonstrates that the observed amplitudes of signals in radial velocity and photometry data are difficult to explain by starspots (Figure 11). Instead, we propose an alternative hypothesis: the radial velocity signal of AD Leo is caused by a planet orbiting the star, locked in spin-orbit resonance.

Typically, such coincidences have been interpreted by simply stating that the radial velocity signal is caused by stellar rotation. However, spin-orbit synchronization might lead to scenarios where such coincidences occur as well (McQuillan et al. 2013; Walkowicz & Basri 2013). According to Walkowicz & Basri (2013), who identified several potential cases in *Kepler* data where stellar rotation periods are equal to or twice the planetary orbital periods, spin-orbit synchronization only happens for planet candidates with radii  $R > 6R_{\oplus}$ , implying that such planets would be closer in radius to Saturn than Neptune. This further suggests that, should AD Leo b exist, it is probably larger than Neptune in radius and thus also more massive than the minimum mass of  $19.7 \pm 1.9 M_{\oplus}$ , as also suggested by the fact that AD Leo is oriented almost pole-on. Given no spin-orbit misalignment and an inclination of  $15.5 \pm 2.5$ , this implies a true mass of  $75.4 \pm 14.7 M_{\oplus}$  or  $0.237 \pm 0.047 M_{\text{Jup}}$ .

Such hot giant planets orbiting M dwarfs—although rare, with an occurrence rate of  $<1\%$  planets per star (Dressing & Charbonneau 2015)—have also been confirmed transiting *Kepler* targets Kepler-45 and Kepler-785 (Johnson et al. 2012; Morton et al. 2016). However, the occurrence rate of short-period giant planets around young, active M dwarfs is not known because the corresponding targets would mostly be selected against when choosing radial velocity targets. The same is the case with *Kepler* transit photometry, for which the automatic data reduction pipelines would likely reject transit signals in spin-orbit resonance cases because of their interpretation as astrophysical false positives (binary stars).

When looking at radial velocities of other similar nearby M dwarfs that are known to be rapid rotators based on detections of photometric rotation periods in ASAS-S *V*-band photometry, such rotation periods do not generally give rise to unique and significant radial velocity signals (Figure 13). AD Leo does not seem to fit into this pattern because the comparison stars that have stable photometric signatures of rotation periods in ASAS data do not show strong evidence for unique periodic signals in their respective radial velocities (Figure 13). Moreover, the rotation-induced radial velocity signal of the slow rotator GJ 674 is not independent of wavelength, indicating that stellar rotation cannot be expected to produce wavelength-invariant radial velocity signals. These results suggest that the radial velocity signal of AD Leo is







probably caused, at least partially, by a planet rather than being exclusively a consequence of stellar rotation.

We considered the possibility that the nearly pole-on orientation makes AD Leo different from the reference targets in Section 7.1. However, this scenario is unlikely because the amplitude of a starspot-induced radial velocity signal is proportional to  $\sin i$  and thus decreases to zero as the inclination of the rotation axis approaches zero. It should therefore be expected that stars that are further from pole-on orientation, i.e., the reference targets for which this is the case on average (assuming random orientation in space), show greater, more easily detectable periodic radial velocity variability caused by corotation of starspots on the stellar surface. Yet the exact opposite is observed.

We consider it unlikely that the unique and time- and wavelength-invariant radial velocity signal of AD Leo at a period of 2.23 days could be caused by stellar rotation. Rather, it seems probable that it is in fact caused by a planet with a mass of  $0.237 \pm 0.047 M_{\text{Jup}}$  orbiting the star. If this interpretation is correct, AD Leo, due to its vicinity with  $d = 4.9$  pc, is an important benchmark target for studying spin-orbit resonances and star-planet interactions in the early stages of stellar evolution. Our results for GJ 674 also suggest that rotation-induced radial velocity signals can be differentiated from Keplerian ones by looking at the dependence of the signals on spectral wavelength.

MT and HRAJ are supported by grants from the Leverhulme Trust (RPG-2014-281) and the Science and Technology Facilities Council (ST/M001008/1). SSV gratefully acknowledges support from NSF grants AST-0307493 and AST-0908870. The work herein is partially based on observations obtained at the W. M. Keck Observatory, which is operated jointly by the University of California and the California Institute of Technology, and we thank the UC-Keck and NASA-Keck Time Assignment Committees for their support. This research has made use of the Keck Observatory Archive (KOA), which is operated by the W. M. Keck Observatory and the NASA Exoplanet Science Institute (NExScI) under contract with the National Aeronautics and Space Administration. We would like to thank Nicholas M. Hunt-Walker for providing the *MOST* data. We also wish to extend our special thanks to those of Hawaiian ancestry on whose sacred mountain of Maunakea we are privileged to be guests. Without their generous hospitality, the Keck observations presented herein would not have been possible. This research has made use of the SIMBAD database, operated at CDS, Strasbourg, France. We are very grateful to the anonymous reviewer who presented suggestions and constructive criticism, greatly improving the paper.

### ORCID iDs

Hugh R. A. Jones  <https://orcid.org/0000-0003-0433-3665>  
 Guillem Anglada-Escudé  <https://orcid.org/0000-0002-3645-5977>  
 R. Paul Butler  <https://orcid.org/0000-0003-1305-3761>  
 Steven S. Vogt  <https://orcid.org/0000-0001-7177-7456>

### References

Adams, F. C., & Bloch, A. M. 2015, *MNRAS*, 446, 3676  
 Anglada-Escudé, G., Arriagada, P., Tuomi, M., et al. 2014, *MNRAS*, 443, L89

Anglada-Escudé, G., Arriagada, P., Vogt, S. S., et al. 2012, *ApJL*, 751, L16  
 Anglada-Escudé, G., & Butler, R. P. 2012, *ApJS*, 200, 15  
 Anglada-Escudé, G., Tuomi, M., Arriagada, P., et al. 2016, *ApJ*, 830, 74  
 Anglada-Escudé, G., Tuomi, M., Gerlach, E., et al. 2013, *A&A*, 556, A126  
 Baluev, R. V. 2009, *MNRAS*, 393, 969  
 Baluev, R. V. 2013, *MNRAS*, 429, 2052  
 Baraffe, I., Homeier, D., Allard, F., & Chabrier, G. 2015, *A&A*, 577, A42  
 Barnes, J. R., Jeffers, S. V., Anglada-Escudé, G., et al. 2017, *MNRAS*, 466, 1733  
 Barnes, J. R., Jeffers, S. V., & Jones, H. R. A. 2011, *MNRAS*, 412, 1599  
 Barnes, J. R., Jeffers, S. V., Jones, H. R. A., et al. 2015, *ApJ*, 812, 42  
 Berdyugina, S. V. 2005, *LRSF*, 2, 8  
 Bonfils, X., Delfosse, X., Udry, S., et al. 2013, *A&A*, 549, A109  
 Bonfils, X., Mayor, M., Delfosse, X., et al. 2007, *A&A*, 474, 293  
 Buccino, A. P., Petrucci, R., Jofré, E., & Mauas, P. J. D. 2014, *ApJL*, 781, L9  
 Butler, R. P., Vogt, S. S., Laughlin, G., et al. 2017, *AJ*, 153, 208  
 Chabrier, G., & Baraffe, I. 2000, *ARA&A*, 38, 337  
 Collier Cameron, A. 2001, in *Astrotomography—Indirect Imaging Methods in Observational Astronomy*, Vol. 573 ed. H. M. J. Boffin, D. Steeghs, & J. Cuypers (Berlin: Springer), 183  
 Cutri, R. M., Skrutskie, M. F., van Dyk, S., et al. 2013, *The IRSA 2MASS All-Sky Point Source Catalog* (Washington, DC: NASA/IPAC Infrared Science Archive)  
 Delfosse, X., Forveille, T., Ségransan, D., et al. 2000, *A&A*, 364, 217  
 Dressing, C. D., & Charbonneau, D. 2015, *ApJ*, 807, 45  
 Engle, S. G., Guinan, E. F., & Mizusawa, T. 2009, in *AIP Conf. Proc.* 1135, *Future Directions in Ultraviolet spectroscopy* (Melville, NY: AIP), 221  
 Feng, F., Tuomi, M., Jones, H. R. A., et al. 2016, *MNRAS*, 461, 2440  
 Feng, F., Tuomi, M., Jones, H. R. A., et al. 2017, *AJ*, 154, 135  
 Feroz, F., & Hobson, M. P. 2013, *MNRAS*, 437, 3540  
 Haario, H., Laine, M., Mira, A., & Saksman, E. 2006, *Stat. Comp.*, 16, 339  
 Haario, H., Saksman, E., & Tamminen, J. 2001, *Bernoulli*, 7, 223  
 Hastings, W. 1970, *Biometrika*, 57, 97  
 Houdebine, E. R., Mullan, D. J., Paletou, F., & Gebran, M. 2016, *ApJ*, 822, 97  
 Hunt-Walker, N. M., Hilton, E. J., Kowalski, A. F., et al. 2012, *PASP*, 124, 545  
 Hut, P. 1980, *A&A*, 92, 167  
 Jenkins, J. S., & Tuomi, M. 2014, *ApJ*, 794, 110  
 Johnson, J. A., Gazak, J. Z., Apps, K., et al. 2012, *AJ*, 143, 111  
 Kaipio, J., & Somersalo, E. 2005, *Statistical and Computational Inverse Problems*, Applied Mathematical Sciences (Berlin: Springer), 160  
 Kass, R. E., & Raftery, A. E. 1995, *J. Am. Stat. Assoc.*, 430, 773  
 Kiraga, M., & Stepien, K. 2007, *AcA*, 57, 149  
 Lomb, N. R. 1976, *Ap&SS*, 39, 447  
 Mayor, M., Pepe, F., Queloz, D., et al. 2003, *ESO Messenger*, 114, 20  
 McQuillan, A., Mazeh, T., & Aigrain, S. 2013, *ApJL*, 775, L11  
 Metropolis, N., Rosenbluth, A. W., Rosenbluth, M. N., et al. 1953, *JChPh*, 21, 1087  
 Morin, J., Donati, J.-F., Petit, P., et al. 2008, *MNRAS*, 390, 567  
 Morton, T. D., Bryson, S. T., Coughlin, J. L., et al. 2016, *ApJ*, 822, 86  
 Neves, V., Bonfils, X., Santos, N. C., et al. 2012, *A&A*, 538, A25  
 Newton, E. R., Irwin, J., Charbonneau, D., et al. 2016, *ApJL*, 821, L19  
 Pojmański, G. 1997, *AcA*, 47, 467  
 Pojmański, G. 2002, *AcA*, 52, 397  
 Reiners, A., Shulyak, D., Anglada-Escudé, G., et al. 2013, *A&A*, 552, A103  
 Robertson, P., Mahadevan, S., Endl, M., & Roy, A. 2014, *Sci*, 345, 440  
 Robertson, P., Roy, A., & Mahadevan, S. 2015, *ApJL*, 805, L22  
 Rojas-Ayala, B., Covey, K. R., Muirhead, P. S., & Lloyd, J. P. 2013, *ApJ*, 748, 93  
 Scargle, J. D. 1982, *ApJ*, 263, 835  
 Schwarz, G. E. 1978, *AnSta*, 6, 461  
 Shkolnik, E., Liu, M. C., & Reid, I. N. 2009, *ApJ*, 699, 649  
 Spiesman, W. J., & Hawley, S. L. 1986, *AJ*, 92, 664  
 Suárez Mascareño, A. S., Rebolo, R., González Hernández, J. I., & Esposito, M. 2015, *MNRAS*, 452, 2745  
 Teitler, S., & Königl, A. 2014, *ApJ*, 786, 139  
 Tuomi, M. 2011, *A&A*, 528, L5  
 Tuomi, M. 2012, *A&A*, 543, A52  
 Tuomi, M., Jones, H. R. A., Anglada-Escudé, G., et al. 2018, *ApJS*, submitted  
 Tuomi, M., Jones, H. R. A., Barnes, J. R., et al. 2014, *MNRAS*, 441, 1545  
 Vogt, S., Butler, P., Rivera, E., et al. 2010, *ApJ*, 723, 954  
 Vogt, S. S., Allen, S. L., Bigelow, B. C., et al. 1994, *Proc. SPIE*, 2198, 362  
 Vogt, S. S., Butler, R. P., & Haghighipour, N. 2012, *AN*, 333, 561  
 Walkowicz, L. M., & Basri, G. S. 2013, *MNRAS*, 436, 1883  
 Winters, J. G., Henry, T. J., Lurie, J. C., et al. 2015, *AJ*, 149, 5  
 Zacharias, N., Finch, C. T., Girard, T. M., et al. 2013, *AJ*, 145, 44